TECHNICAL UNIVERSITY OF LIBEREC
Faculty of Mechanical Engineering

Cavitation microjet and shock wave in a signal from impact load measurement

Master Thesis

Study programme:	N2301 Mechanical Engineering
Study branch:	Machines and Equipment Design
Author:	**Nugzari Kardava**
Thesis Supervisors:	Ing. Jan Hujer, Ph.D. Department of Power Engineering Equipment

Liberec 2021

TECHNICAL UNIVERSITY OF LIBEREC
Faculty of Mechanical Engineering

Master Thesis Assignment Form

Cavitation microjet and shock wave in a signal from impact load measurement

Name and surname: **Nugzari Kardava**
Identification number: S19000372
Study programme: N2301 Mechanical Engineering
Study branch: Machines and Equipment Design
Assigning department: Department of Power Engineering Equipment
Academic year: **2020/2021**

Rules for Elaboration:

Cavitation cause a damage of turbomachines. During a collapse of cavitation bubble, two phenomena – cavitation microjet and shock wave, impact and erode close wall. PVDF sensor fixed on the wall can be used for a measurement of phenomena impacts which are somehow superimposed in a measured signal. The aim of this thesis is to test whether is possible to identify phenomena in a signal and separate their individual impact.
Thesis will follow these steps:
1. Literature review on a cavitation bubble interaction with the close wall, measurement in the field of thesis topic and appropriate sensors.
2. Design of an experiment with a PVDF sensor.
3. Realization of the experiment and acquisition of collapsing bubble signals.
4. Analysis of measured data.
5. Discussion.

Scope of Graphic Work: –
Scope of Report: 60
Thesis Form: printed/electronic
Thesis Language: English

List of Specialised Literature:

Kim, K. H., Chahine, G., Franc, J.-P. & Karimi, A. (2014) *Advanced experimental and numerical techniques for cavitation erosion prediction*. Dordrecht, Springer.
Franc, J.-P. & Michel, J.-M. (2004) Fundamentals of cavitation. Dordrecht, Kluwer.
Franc, J.-P., Riondet, M., Karimi, A. & Chahine, G. (2011) Impact load measurement in an Erosive Cavitating Flow. Journal of Fluids Engineering. 133, 121301-1.
Momma, T. & Lichtarowicz, A (1995) A study of pressures and erosion produced by collapsing cavitation. Wear. 186-187, 425-436.
Wang, Y. C. & Chen, Y. W. (2007) Application of piezoelectric PVDF film to the measurement of impulsive forces generated by cavitation bubble collapse near a solid boundary. *Experimental Thermal and Fluid Science*. 32, 403-414.
Piezo Film Sensors Technical Manual (1999), Norrsitown, Measurement Specialties.

Thesis Supervisors: Ing. Jan Hujer, Ph.D.
Department of Power Engineering Equipment

Date of Thesis Assignment: November 1, 2020
Date of Thesis Submission: April 30, 2022

L.S.

prof. Dr. Ing. Petr Lenfeld
Dean

doc. Ing. Petra Dančová, Ph.D.
Head of Department

Liberec November 1, 2020

Declaration

I hereby certify, I, myself, have written my master thesis as an original and primary work using the literature listed below and consulting it with my thesis supervisor and my thesis counsellor.

I acknowledge that my bachelor master thesis is fully governed by Act No. 121/2000 Coll., the Copyright Act, in particular Article 60 – School Work.

I acknowledge that the Technical University of Liberec does not infringe my copyrights by using my master thesis for internal purposes of the Technical University of Liberec.

I am aware of my obligation to inform the Technical University of Liberec on having used or granted license to use the results of my master thesis; in such a case the Technical University of Liberec may require reimbursement of the costs incurred for creating the result up to their actual amount.

At the same time, I honestly declare that the text of the printed version of my master thesis is identical with the text of the electronic version uploaded into the IS/STAG.

I acknowledge that the Technical University of Liberec will make my master thesis public in accordance with paragraph 47b of Act No. 111/1998 Coll., on Higher Education Institutions and on Amendment to Other Acts (the Higher Education Act), as amended.

I am aware of the consequences which may under the Higher Education Act result from a breach of this declaration.

June 3, 2021 Nugzari Kardava

ABSTRACT

This master thesis work is done to try and describe processes that occurred during cavitation bubble collapse near a solid boundary, to try and separate cavitation microjet and shock wave impact from the signal received by PVDF sensors. The thesis starts with the introduction of the general terms connected to the cavitation phenomenon itself. Literature related to the bubble interaction phenomena near solid wall and usage of PVDF films is also reviewed. The experimental setup, with the method of bubble generation and used equipment are also described. Two PVDF sensors were fixed to two metal plates in order to receive signals from the bubble collapse, generated by the underwater spark discharge. Calibration of the sensors was done with the ball drop method. The experiments were observed by the Nanosense MKIII CCD camera at 10000 fps. Bubbles were generated at different dimensionless stand-off distances γ and impacts were further analyzed and compared to different articles. A small chapter is also dedicated to describe the possible problems that can occur during the experiments using PVDF films.

Inverse squares law was used to check if the theoretical and experimental shock wave propagation were the same. This law works only for spherical shock sources, results of the experimental values during specific γ ranges are in the acceptable level with the theoretical model. Maximum impact forces and loading stresses (pressures) are shown and discussed. The exact values of the cavitation microjet are not recorded as a significant event, but several important assumptions were made, especially when the dimensionless stand-off (proximity) parameter γ is in the range between 0.8 and 1. Double peak-shaped signals are received in this range and these peaks are created by the splash effect (accompanied by the shock waves) due to the microjet and by the moving flow towards the ring (as well can be interpreted as a bubble ring collapse).

Keywords: cavitation, cavitation bubble, bubble collapse, shock waves, microjet, PVDF sensor.

ACKNOWLEDGMENTS

I wish to express my deepest gratitude to my supervisor Ing. Jan Hujer Ph.D. for his guidance, advice, support and spent time with me in the laboratory, it was a huge help for me throughout all the master's thesis work. I would also like to thank all the academic staff and personnel of TUL who helped me during the last 2 years. I am very grateful to the Ministry of Youth and Sport of the Czech Republic for awarding me with state scholarship and giving me the possibility to study at the Technical University of Liberec. It's been a very interesting journey.

Lastly, I would like to express my gratitude and love to my fiancée and family, for their support and encouragement during my study period in the Czech Republic. This thesis is in memory of my grandfather, Valeri Kankia, who taught me fundamental principles in life, which helped me to become the person I am now.

This work was supported by the Student Grant Competition of the Technical University of Liberec under project No. SGS-2020-5028.

`

TABLE OF CONTENTS

`

`

LIST OF THE FIGURES

`

LIST OF THE TABLES

`

LIST OF SYMBOLS AND ABBREVIATIONS

Symbol	Description	Unit
R	Bubble radius	[m]
R_{max}	Maximum bubble radius	[m]
R_0	Initial bubble radius	[m]
$\dot{R}$	First order derivative of bubble radius	[m/s]
$\ddot{R}$	Second order derivative of bubble radius	[m/s^2]
p	Pressure	[Pa]
p_v	Vapor pressure inside the bubble	[Pa]
p_∞	Liquid pressure at an infinite distance from the bubble	[Pa]
p_{g0}	Pressure of gas at initial state	[Pa]
S	Surface tension	[N/m]
ρ	Density of the liquid	[kg/m^3]
y	Polytropic exponent of the gas	[-]
μ	Dynamic viscosity?	[Pa.s]
τ	Rayleigh time	[s]
τ	Impact time	[s]
Π	non-dimensional pressure	[-]
v_j	Microjet velocity	[m/s]
c_l	Speed of sound for liquid	[m/s]
ρ_s	Density of the solid wall	[kg/m^3]
c_s	Speed of sound for solid wall	[m/s]
d_{31}, d_{33}	Piezo strain constant	[C/N]
g_{31}, g_{33}	Piezo stress constant	[Vm/N]
C	Capacitance	[pF]
f_r	Resonance Frequency	[kHz]
$\varepsilon_{r,}$	Relative permittivity	[F/m]
ε_0	permittivity of free space	[F/m]
t_f	Thickness of PVDF film	[µm]
A	Area	[m^2]
F_{mean}	Mean impact force	[N]
F_{max}	Maximum impact force	[N]
v	velocity	[m/s]
h	Height	[m]
V	Voltage	[V]
I	Intensity of shock wave	[W/m²]
X	Mechanical stress (pressure) on the PVDF film	[Pa]
L	Distance from the PVDF sensor	[m]
γ	Dimensionless stand-off parameter (or proximity parameter)	[-]

`

LIST OF ABBREVIATIONS

DAQ	Data Acquisition
DC	Direct Current
LIB	Laser Induced Breakdown
PVDF	Polyvinylidene Fluoride
CCD	Charge - Coupled Device
MSI	Measurement Specialties Inc.
NI	National Instruments
PXI	PCI Extensions for Instrumentation
PCI	Peripheral Component Interconnect
LED	Light Emitting Diode
LCD	Liquid Crystal Display

`

1. INTRODUCTION

Cavitation is the formation of vapor bubbles inside a liquid at low-pressure areas that arise in locations wherein the liquid has been increased to excessive velocities, as withinside the operation of pumps, turbines, and marine propellers. Cavitation can be the reason of the erosion, increased vibrations and lower performance in mentioned equipment. The cavities form while the pressure of the liquid has been decreased to its vapor pressure; they increase because the stress is, in addition, decreased together with the flow and suddenly, fall apart after they attain areas of higher pressure. The unexpected increase and collapse of those vapor cavities motive the intense pressures that pit the steel surfaces uncovered to the cavitating liquid [1].

Cavitation is triggered withinside the low-stress area as an explosive boom of microscopic nuclei into a whole lot of large bubbles. These are then transported with the aid of using the liquid towards areas of better stress wherein they collapse. This collapse is normally very violent and is observed with compression of its content material and the next emission of a massive amplitude stress (shock) wave. Furthermore, if the bubble collapses near the boundary when the distance is smaller than twice its radius, microjet forms. If the impulsive stress ensuing both from the effect of the microjet or from the effect of the surprise waves exceeds some suitable fabric threshold, together with its yield pressure or its ultimate strength, neighborhood harm is induced [2].

The ways to study the effects of bubble collapse in a controlled conditions can be by generating cavitation nuclei by laser, spark, etc. Dimensionless proximity (stand-off) parameter, which is the ratio between the distance from the boundary and maximum bubble radius ($\gamma=L/R_{max}$) has significant importance in the whole bubble collapse process, accompanied with different effects.

As mentioned above, during cavitation bubble collapse, two phenomena- microjet and shock waves can occur, they impact and erode close to the wall and since it's a very rapid process, special types of equipment are needed to observe it. PVDF sensor fixed on the wall can be used for measurement of phenomena somehow superimposed in a measured signal. The aim of this thesis is to test whether is possible to identify phenomena in a signal and separate their individual impact.

`

1.1 Definition of Cavitation

Cavitation is the existence of vapor cavities in an originally homogeneous liquid and it can be defined as the breakdown of a liquid medium under very low pressures [3] and it is a desirable field for continuum mechanics, it applies to cases when liquids are static as well as when it is in motion. The cavities can be either field with a gas/vapor or void. In liquid flows, the phase change is happening due to high velocities which stimulate low pressures. Liquid vaporization happens in the presence of cavitation microbubbles called "cavitation nuclei". The behavior of cavitation can be described using a phase diagram of water, shown in Figure 1.1. Pressure, *p* and temperature, *T* can be used to define liquid state. Vaporization can happen either by increasing temperature while pressure stays constant (boiling) process 1-3, or due to significant pressure drop during constant temperature (cavitation) process 1-2. In the figure, T_r represents a temperature corresponding to the triple point and T_c corresponding to a critical point.

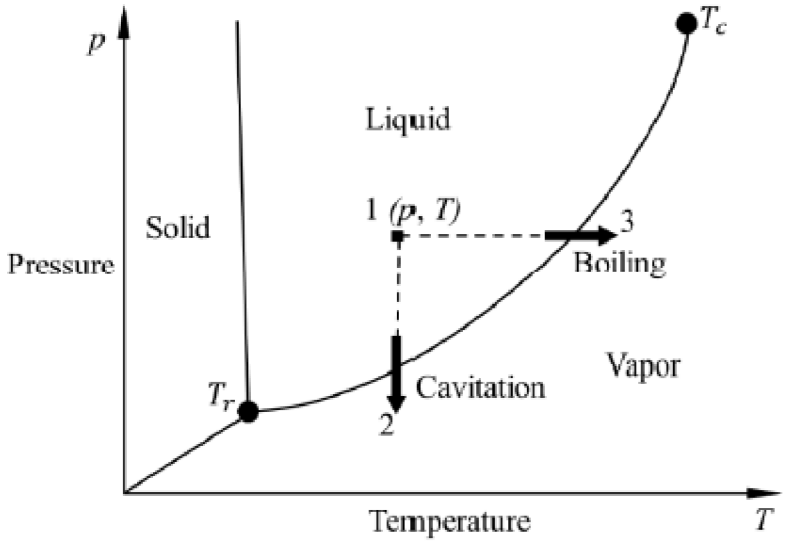

Figure 1-1. Phase change of water [4]

Formation phases of cavities are - nucleation and growth. During nucleation, new nuclei are formed in the liquid, which was homogeneous previously. The expansion of nuclei to a macroscopic size is called bubble growth. Exists two types of nucleation processes: homogeneous and heterogeneous. During homogeneous nucleation, nuclei can be formed instantly by the result of molecular fluctuation or molecular interaction. During heterogeneous cavitation, nuclei are formed between the boundary of the liquid and solid wall.

The cavitation generated by the absorption of highly concentrated light in a liquid is very closely associated with the term laser-induced breakdown (LIB) [5]. It causes dielectric breakdown due to ionization of a different state of substance through absorption of thermal or electromagnetic energy.

`

1.2 Classification of Cavitation

Different types of cavitation can be developed in any kind of liquid flow [3]. It is a complex phenomenon because it includes a lot of aspects, which occur in many fields, such as hydraulic engineering, mechanical engineering, medical industry, etc. Cavitation erosion takes place when mechanical energy concentrates on very small areas.
Cavitation can be classified by the content of the bubble. Vaporous cavitation happens when the vapor-filled bubble is created by the local static pressure drops below the saturated vapor pressure during a constant temperature. On the other hand, gaseous cavitation occurs when the local static pressure drops under the saturation pressure of the no condensable gas resolved in the liquid. The amount of the gas which can be resolved in the liquid under a given pressure is given by Henry's law [6].
The fast growth of tiny air nuclei in a low-pressure area creates transient isolated bubbles. They move with the main flow and disappear after they enter areas of high enough pressure. Attached or sheet cavities can occur to the low-pressure side of bodies such as blades and foils. Cavitating vertices are seen in turbulent wakes, propeller blade tips, and other regions [3].
Hydrodynamic cavitation - occurs when the liquid flows through a region of lower pressure, e.g., in accelerated flow inside some equipment, such pumps or rotating propellers[5]. The pressure of the fluid decreases due to speed increase and after it becomes smaller than vapor pressure, liquid vaporizes.
Acoustic cavitation is the formation and aggressive collapse of bubbles in liquid irradiated with intense ultrasound [7]. During ultrasonic wave rarefaction, the pressure near the wall of the bubble is higher than a liquid pressure far from the bubble, and therefore small bubbles are expanding, on the other hand, during the compression phase, bubbles collapse and shockwaves are created. Liquid jet penetrates into the bubble, causing erosion.
Optic cavitation happens when photons of high-intensity laser are focused on the liquid, fracturing it and creating bubbles, it increases in size until some point and then it collapses. To say in other words, the optical breakdown has happened after which shockwave was produced. This method is often called laser-induced cavitation.
Particle cavitation means that cavitation is caused by the elementary particles, which went through the liquid and created an ionization trail. These ions transmit energy to electrons which gives up to around 1000 electron volts of energy in a small volume causing rapid local heating [8].
Traveling cavitation occurs by individual transient bubbles that form in the fluid, enlarge, diminish, and then collapse [9]. This type of cavitation can be observed on propeller as a tiny angle of incidence.

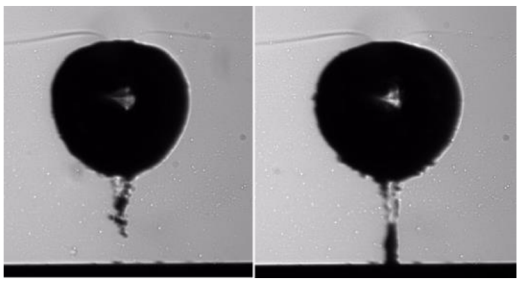

Figure 1-2. A bubble generating a liquid jet against the solid wall during the collapse [5].

`

1.3 Effects of Cavitation

1.3.1 Negative Effects of Cavitation

Fluid operating in a hydrodynamic system is generally assumed to be homogeneous. Problems due to cavitation occur in turbomachinery, pumps, etc. Cavitation can be the reason of significant damage to material surfaces like erosion, vibration and noise. The reasons of erosion are impact loads created during bubble collapse near the wall, as we know bubbles created in low-pressure regions are transported by the liquid towards to high-pressure area where they collapse. Liquid jet and shockwaves are two main reasons for erosion (see Figure 1-2)[5]. If the impulsive impact pressure, caused by one of them, is higher than some material limit (like yield stress or tensile strength) damage happens [2]. Damage of the naval ship rudder, caused by cavitation is seen in Figure 1-4.

Cavitation in pumps occurs due to the pressure decrease of the flowing liquid. Pressure change, inside the pump, turns liquid into vapor, in the opposite, impellers spin turns them back to liquid. If the cavitation is strong enough, it can damage the impeller surface and inlet, accordingly, pump performance decreases [10]. Cavitation often occurs in centrifugal pumps, where the flow area of the eye of impeller is smaller than the flow area of the pump suction or impeller vanes. This means that in centrifugal pumps cavitation performance mostly depends on the impeller geometrical design [11]. In a Figure 1-3. Cavitation erosion in a centrifugal pump impeller you can see result of cavitation erosion in a centrifugal pump.

Cavitation is the problem of reaction-type turbines and it occurs mainly around the runner and in the draft tube. Reduction of cavitation can be achieved by design modifications or improving the quality of coatings of welded parts.

Cavitation mostly occurs on the low-pressure side of the runner blades. In hydraulic equipment, cavitation impact can have different forms, which is dependent on the working conditions of machine and its design. It is hard to avoid effects of cavitation fully in hydraulic turbines but can be reduced to an economically acceptable level [12].

Figure 1-3. Cavitation erosion in a centrifugal pump impeller.

Figure 1-4. Cavitation effects on the rudder of a ship.

`

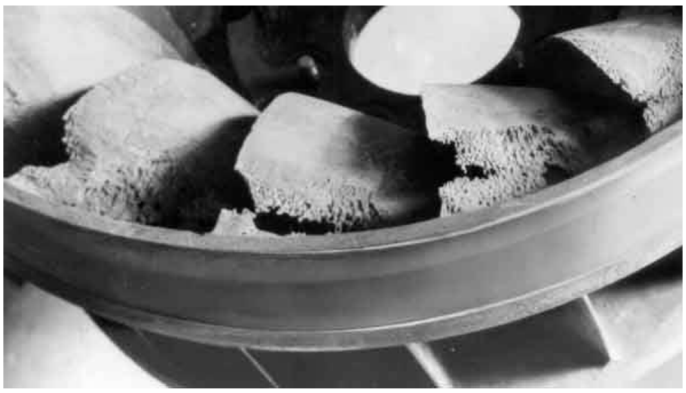

Figure 1-5. Cavitation damage on the blades of a Francis turbine [13].

1.3.2 Positive Effects of Cavitation

Despite all the negative effects mentioned above, cavitation can still be beneficial especially in the field of medicine. Cavitation by Lithotripter Shock Waves bubble clusters were used to break kidney stones. Their collapse caused the disintegration of the driving side of the stone and the collapse of clusters at the sides of stones showed up to contribute to the development of splits [14].

Furthermore, cavitation can be generated using a laser beam. Bubbles made by laser light centered on an indicated locale, can cut through tissue and hence produce the exact microscopic opening which is potentially very beneficial for surgeries. Cancer cells can also be treated with liposomes and ultrasounds [15].

Cavitation shotless peening is a modern technique for surface improvement of metallic materials. Cavitation impact is caused due to high-speed cavitation jets. Bubble collapse creates plastic deformation on the surface, which acts as a compressive layer that impedes fatigue crack initiation, as well as improves the strength of the material [16].
Acoustic cavitation is frequently used and approved method for the cleaning of wastewater. Hydrodynamic cavitation can be used for the removal of pharmaceuticals, toxic cyanobacteria, green microalgae, bacteria and viruses from water and wastewater [17].

1.4 Dynamics of Cavitation Bubble

Cavitation Bubbles can be considered either spherical or non-spherical. The model of dynamic evolution of spherical bubble with a fixed center is a simple way to see main features of bubble collapse, bubble formation from nucleus and its oscillation. In order, to understand how bubbles were behaving, Besant in 1859, firstly considered liquid motion induced by a spherical cavity in an infinite medium under uniform pressure at infinity. In 1917 Rayleigh solved it for non-viscous liquid to describe cavitation erosion phenomenon, in 1948 Cole used the model and applied it to sub-marine explosions and later, in 1954

`

Plesset considered the general case of bubble evolution for a viscous and non-compressible liquid [3].

Several assumptions and simplifications were made for this process, such as: liquid has to be incompressible and either Newtonian or inviscid, gravity has to be neglected, air content of the bubble is constant and inertia is neglected as well as heat exchanges on the surroundings [3]. Furthermore, bubble always remains its spherical body while changing radius, center is fixed in space and bubble is stationary, bubble content is homogeneous [5].

The most common way used to define the development of the radius R and pressure in the liquid is Rayleigh-Plesset equation (1). It is used to determine the behavior of the spherical bubble in incompressible non-viscous liquid:

$$\rho\left(R\ddot{R} + \frac{3}{2}\dot{R}^2\right) = p_v - p_\infty(t) + p_{g0}\left(\frac{R_0}{R}\right)^{3y} - \frac{2S}{R} - 4\mu\frac{\dot{R}}{R} \ . \tag{1}$$

where ρ is density of the liquid, R is bubble radius at time t, $\dot{R}$ and $\ddot{R}$ are 1st and 2nd order derivatives of bubble radius with respect of time, R_0 is the initial bubble radius, p_v is the internal vapor pressure of the bubble, $p_\infty(t)$pressure far distance from bubble, y polytropic exponent of the gas, p_{g0} the pressure of gas inside the bubble at initial state and S is the surface tension.

For the big bubble, when the effects on non-condensable gas, surface tension and viscosity can be of no importance, Rayleigh-Plesset equation can be written as a basic Rayleigh equation (*2*):

$$\rho\left(R\ddot{R} + \frac{3}{2}\dot{R}^2\right) = p_v - (t) \ . \tag{2}$$

If the applied pressure p_∞ is constant, integrated equation will look like this:

$$\dot{R}^2 = \frac{2}{3}\frac{p_v - p_\infty}{\rho}\left(1 - \left(\frac{R_0}{R}\right)^3\right) \tag{3}$$

When $p_\infty$is less than p_v, Bubble radius R will become more than initial radius R_0. Bubble growth rate can be written as:

$$\dot{R} \cong \sqrt{\frac{2}{3}\frac{p_v - p_\infty}{\rho}} \ . \tag{4}$$

When $p_\infty$is greater than p_v, bubble size decreases. During bubble collapse, effects of viscosity, non-condensable gas and surface tension are still negligible and decrease rate will be:

$$\dot{R} \cong \sqrt{\frac{2}{3}\frac{p_v - p_\infty}{\rho}}\left[\left(\frac{R_0}{R}\right)^3 - 1\right]. \tag{5}$$

`

During bubble collapse, radius R can be considered as zero and collapse time can be obtained. The collapse time τ is known as the Rayleigh time (*6*):

$$\tau \cong 0.915\, R_0 \sqrt{\frac{\rho}{p_\infty - p_v}}\ . \tag{6}$$

In this time, bubble fully disappears after which rebound process starts [18].

1.5 Cavitation Pressure Field [3]

From the equations above, we can determine pressure field *p(r,t)* value of $\ddot{R}$ will be derived to the result:

$$\ddot{R} = \frac{p_\infty - p_v}{p_\infty - p_v} \cdot \frac{{R_0}^3}{R^4}\ . \tag{7}$$

So the result, Π (non-dimensional pressure) will be:

$$\Pi\,(r,t) = \frac{p(r,t) - p_\infty}{p_\infty - p_v} = \frac{R}{3r}\left(\frac{{R_0}^3}{R^4} - 4\right) - \frac{R^4}{3r^4}\left(\frac{{R_0}^3}{R^4} - 1\right) \tag{8}$$

Maximum pressure is:

$$\Pi_{max} = \frac{p_{max} - p_\infty}{p_\infty - p_v} = \frac{\left(\frac{{R_0}^3}{4R^3} - 1\right)^{4/3}}{\left(\frac{{R_0}^3}{R^3} - 1\right)^{1/3}}\ . \tag{9}$$

The distance r_{max}, in where this maximum pressure is obtained is can be written as:

$$\frac{r_{max}}{R} = \frac{\left(\frac{{R_0}^3}{R^3} - 1\right)^{1/3}}{\left(\frac{{R_0}^3}{4R^3} - 1\right)}\ . \tag{10}$$

When R/R_0 becomes small, equations can be rewritten as:

$$\Pi_{max} = \frac{1}{4^{4/3}}\left(\frac{R_0}{R}\right)^3 = 0.157\left(\frac{R_0}{R}\right)^3. \tag{11}$$

`

$$\frac{r_{max}}{R} = \sqrt[3]{4} \cong 1.59 \ . \tag{12}$$

In this model, only pressure and inertia are foreseen, but it gives us possibility to detect several main characteristics of the pressure, created by bubble collapse. The internal pressure of the bubble doesn't change and doesn't have effect on resistance to liquid motion, but if the bubble contains some amount of non-condensable gas, compression will occur during bubble collapse and it will resist liquid motion. In Figure 1-6, from the book "Fundamentals of Cavitation" - by Franc J.P. you can see different values of non-dimensional pressure Π [3].

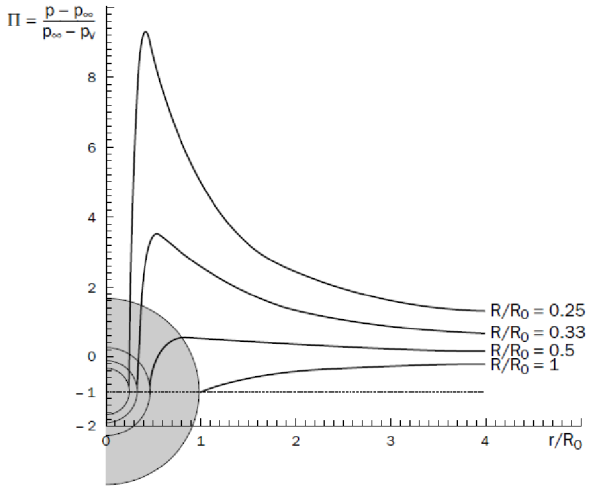

Figure 1-6. Non-dimensional pressure distribution in the liquid during the collapse of the bubble [3].

1.6 Cavitation Bubble Collapse and Impact Load near a Rigid Wall

As already been mentioned, cavitation bubble collapses in the high-pressure region. As a result of pressure differences bubble accelerates towards the solid wall. This collapse is very violent and it can be accompanied by compression of its content following by the emission of big amplitude pressure waves. Impacts of the wall, can be also caused by the re-entrant jet, formed in closer distances from the wall [2].

Main reasons of cavitation damage are microjets, splashing effect and shock waves. Back in 1917, Rayleigh has theoretically explained the generation of shock waves, while Harrison found some experimental evidence in 1952 [4] [19]. Kornfeld & Suvorov were the first who introduced the thought of microjet hitting the solid wall [4] [20]. Splashing is the secondary evaporation process when, after the microjet, flow moves radially [21]. Tong et al., [22] found that the hydrodynamic pressure produced on the solid boundary by the splash is greater than that of the microjet [8].

The connection between microjet/shock wave and rigid wall can be described by using the water-hammer phenomenon:

`

$$P_{imp} = \frac{\rho_l c_l v_j}{1 + \frac{\rho_l c_l}{\rho_s c_s}} \ . \tag{13}$$

Where, v_j is microjet velocity, ρ_l, c_l are density and speed of sound for liquid and consequently ρ_s, c_s for solid wall [4].

Nowadays, it's known that the microjet velocity, v_j, can be hundreds of m/s. The pressure rise caused by these microjets can be calculated by using Joukowski and Allievi water-hammer formula[3]:

$$\Delta p = \rho c v_j \ . \tag{14}$$

`

Typically, $\Delta p = 150\ MPa$, for water, i.e the same order of magnitude as pressure wave. Both hydrodynamic mechanisms, microjets and shockwaves create high pressure pulses, which can be similar to yield stress of metals [3].

Rayleigh developed an equation for estimation of the pressure, generated from bubble collapse, with radius R, during the time, when microjet was hitting the wall [8] [23]:

$$\frac{p'^2}{2\beta} = \frac{1}{2}\rho U^2 = \frac{P}{3}\left[\left(\frac{R_0}{R}\right)^3 - 1\right] \ . \tag{15}$$

In Figure 1-7, when minimum pressure is lower than critical pressure, bubble grows rapidly (red curve) and its radius exceeds the initial radius, when $P_{min} > P_{cr}$ radius practically remains the same (blue curve).

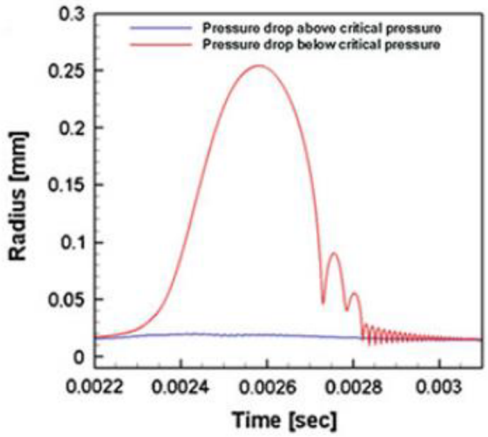

Figure 1-7 . Bubble radius and time dependence in a propeller flow field [2].

Shock wave impacts a solid wall strongly. When it has an elastic type of behavior, the wall shrinks, and shock wave intensity is decreased and the incident wave is partly transmitted and partly reflected by the solid [3]. The intensity of shock waves is dependent on the distance from the wall. Shock waves and microjets can occur together. It usually, happens,

`

when the bubble touches the wall during maximum expansion [24]. After the first shock wave, the collapse of the bubble leads to another (collapse) shock wave. The reason of this phenomena, is that the gas contents of the bubble are highly compressed [4]. Phillipp and Lauterborn made experiments of these types of shock waves, with two different positions from the wall and found out that as intensity is reduced with the decrease of distance, collapse tends to be asymmetrical [4].

Jing Luo and Zhipan Niu conducted an experiment to find out the characteristics of two cavitation bubble collapse near the wall [25]. In Figure 1-8a, single bubble collapse is represented. Figure 1-8b shows us the situation, when two bubble collapse, generated at the same time, while on Figure 1-8c there are two cavitation bubbles generated at different time. From Figure 1-8a, it is visible that no jet is formed, and shock wave shape is practically the sphere. Collapse shock wave, on the Figure 1-8b, forms from the larger bubble. The collapse shock wave, of the earlier developed bubble (c_1-c_4), increases independently from the second cavitation bubble, which was generated at later (c_5-c_8). On the other hand, we can see two shock waves released from the second bubble, for a short period of time (c_8).

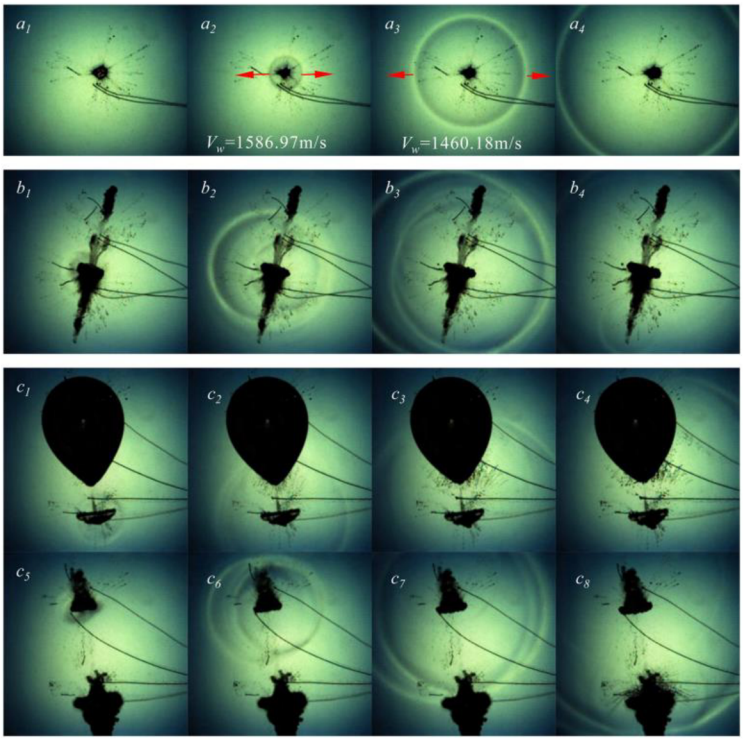

Figure 1-8. Shock wave formed by
collapse of two cavitation bubbles [25].

From this experiment, we can say that initial moment of cavitation bubble, has a very big influence on collapse shock wave. For the cavitation bubbles, developed at same time, the reason of the formation of shock wave is larger bubble and for bubbles, generated at different time the two bubbles have shock wave from the collapse, after one another. Shock waves, in both cases are radically different from the single bubble collapse shock wave[25].

`

1.7 Objective of this Work

As mentioned above, during cavitation bubble collapse, two phenomena - microjet and shock waves can occur, they impact and erode close to wall and since, it's a very rapid process, special types of equipment are needed to observe it. PVDF sensor fixed on the wall can be used for a measurement of phenomena somehow superimposed in a measured signal. The aim of this thesis is to test if it is possible to identify phenomena in a signal and separate their individual impact.

Principles to achieve this goal, are following:

- Research and review bubble interaction phenomena near the solid wall, appropriate measuring devices for this topic and measurement in the field of thesis.
- Design of an experiment using PVDF sensors.
- Calibration and testing of required PVDS Sensors.
- Realization of the experiment, acquisition of collapsing signals for different distances between the PVDF sensors.
- Analysis of measured data.
- Results and discussions.

2. REVIEW OF RELATED LITERATURE

This chapter includes general information about piezoelectric film sensors, areas of their usage, types, production and ways in which they are used and current knowledge about the generating cavitation bubbles and measurements of different types of impact loads.

2.1 Piezoelectric Film Sensors and Their Production

Piezoelectric effect, which is the generation of an electrical charge by the applied mechanical stress or pressure, firstly was discovered by the Curie brothers, in 1880. It took almost 40 years after that to start practical experiments and applications of piezoelectric transducers. In 1918 Langevin, made a quartz transmitter and obtained an underwater sound signal [26]. In the following years, researchers were investigating several piezoelectric properties and materials, but one of the most important moments was when Kawai discovered very high piezoelectricity in the polyvinylidene fluoride (PVDF). It is a semicrystalline polymer and approximately 50% of it is lamellar crystals [27]. It has higher piezoelectric properties than a lot of other materials previously discovered or used. This is due to the PVDF's high dielectric constant. It also has a good ability to absorb certain infrared wavelengths. Newly developed copolymers made it possible to further develop to use of PVDF sensors, because of the improved properties, shapes, etc. Piezoelectric film is very flexible and lightweight. It has a lot of advantages, such as: wide frequency range, low acoustic impedance, which is really close to water, wide dynamic range for pressure, good material properties, low density and high sensitivity, it doesn't have limitations for usage in different applications and can directly be attached to different kinds of structures [26].

`

Piezoelectric sensors are used in different applications. In 2018, Hu et al., designed and fabricated a PVDF sensor to detect wrist motion signals (Figure 2-1). Their sensor has seven layers and the main materials were PDVF film, silicone rubber, PET film and Printed Circuit board (PCB) [28]. From their experiment, it is visible that, the sensitivity of the sensor is always on the level of 3.10 pC/N if the excitation signal is more than 15Hz. Advantages for this type of wrist sensor are that it can measure motion signals which have low frequency, amplitude and etc.

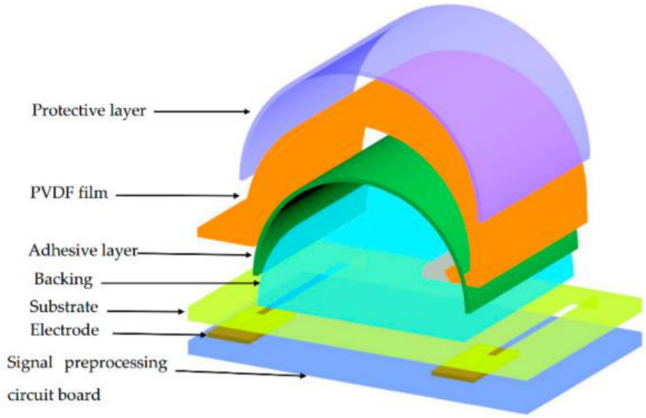

Figure 2-1. Structure diagram of wrist PVDF sensor [28]

In 2019, Cong et al., developed PVDF sensor array (Figure 2-2) to detect dynamic pressure field of the blade tip inside the compressor [29]. Improve of compressor's performance and range of use, is very important problem in today's world. It is not easy to measure blade tip flow field pressure, because of its very small size, also there are more obstacles, such as complicated casing and etc. In this experiment, used PVDF sensor had 40 sensing points, fabricated directly on 30 μm thick PDVF film. Test pressure was up to 3.5 kPa and frequency was 20 kHz. Received results show that PVDF sensor arrays are able to determine pressure field over the tip of the blade and it can be used for complex shaped spatial surfaces or thin-walled structures [29].

2.1.1. PVDF Sensor array, Wang et al., [30]

PVDF sensor array created by Wang et al, in 2005 was used to study the characteristics of impulsive pressure. The reason for their work was to develop an array (Figure 2-3) capable to measure spatial distribution and variation of pressure field, generated from bubble collapse.

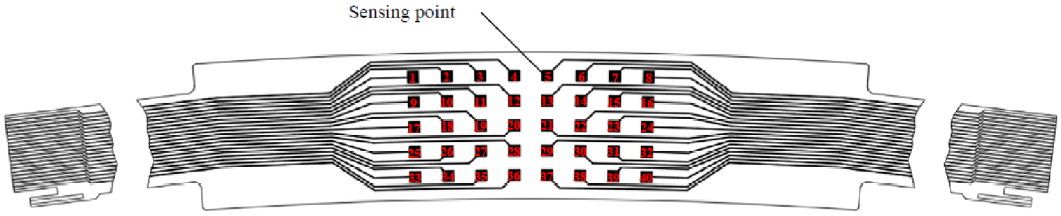

Figure 2-2. Sketch diagram of the PVDF sensor array [29]

`

They have used 25 μm thick aluminum-metalized polarized PVDF film (FV301926, Goodfellow Cambridge Ltd, UK), which was produced by an excimer laser (PS-2000), emitting KrF ultraviolet light pulses up to 350 mJ and duration of 30 ns. The resonance frequency of the used PVDF film was about 22 MHz. Sensing elements, used in this work, were too small, hence their capacitance was only about 100 pF (at 2 kHz). The low-end cut-off frequency for a load of 1 MΩ resistance was 1.6 kHz, so all output signals smaller than that would be reduced. To solve this problem, a buffer circuit, which converts high output impedance into low impedance, shown in Figure 2-4 was designed, each sensing element had its operational amplifier to eliminate the loading effect (AD843JR, Analog Devices, Inc.)

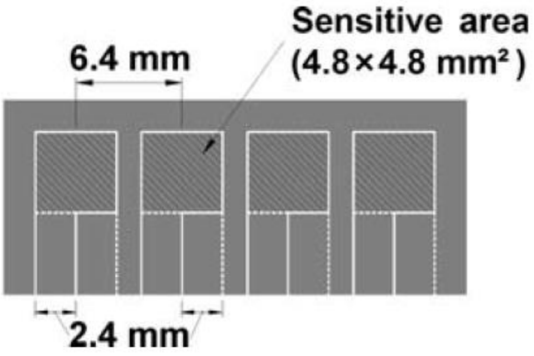

Figure 2-3. Layout of the PVDF array sensor [30].

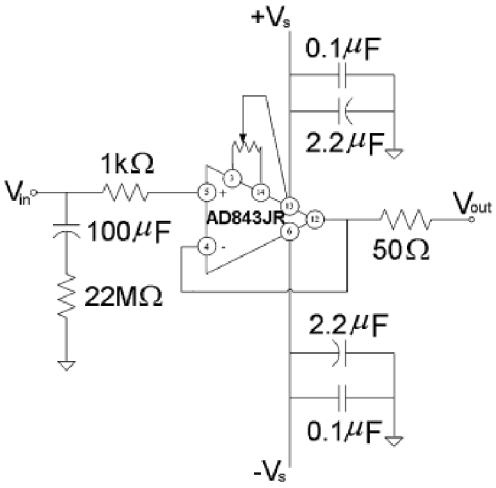

Figure 2-4 Buffer circuit [30].

Sensor calibration was achieved by a gas shock tube. The average response time of PVDF sensors, to the gas shock was 31 ns. From this experiment, it's clear that shock waves are generated after the bubble collapse, not matter what the value of stand-off parameter γ is. The speed of shock waves is dependent on the space and time differences of the signals between the sensors.

2.2 Piezoelectric Film Basic and Operating Properties

Due to the good mechanical and electrical properties, piezoelectric film sensors become more and more popular each year. The fields of its usage are increasing and a lot of applications are created with PDVF films. As we mentioned before, low acoustic impedance, density, good sensitivity and mechanical toughness are advantages of it. In table 1 you can see comparison of properties between PVDF and piezoelectric ceramics material [26].

`

Table 1. Comparison of Piezoelectric Materials [26]

Property	**Units**	**PVDF Film**	**PZT**	**$BaTi0_3$**
Density	10^3 kg/m^3	1.78	7.5	5.7
Relative Permittivity	$\varepsilon/\varepsilon_0$	12	1200	1700
d_{31} Constant	10^{-12} C/N	23	110	78
g_{31} Constant	10^{-3} Vm/N	216	10	5
k_{31} Constant	% at 1 KHz	12	30	21
Acoustic Impedance	10^6 kg/m^2-sec	2.7	30	30

Operating properties of the piezoelectric include: Electro-Mechanical conversion, Mechano-Electrical conversion, Pyro-Electrical conversion, Capacitance, Maximum Output Voltage, Maximum Applied Force, etc. [26]. Piezo film, is not able to capture large displacement of the forces, because frequency below 500 Hz is limited, even for large piezo films, but on the other hand, situation is opposite for the ultrasonic frequencies, as it's seen in modern medical ultrasonic applications, where low frequency response is very good.

Sensitivity of piezoelectric films, as a receiver of mechanical work input are great [26]. The film acts like dynamic strain gage, without necessity of external power and generates better signals. Such good sensitivity is achieved by the low thickness, therefore a small cross-sectional area, as short longitudinal forces create large stress. Furthermore, if additional laminated element is places in between two layers of the material, contractive forces can be converted into even longer longitudinal forces.

In case of pyro to electrical conversion, attention needs to be paid on design of low frequency (<0.01. to 1 Hz) sensors, because temperature changes can overflow of the output of pyro-generated signal. In such cases, film can generate a voltage according to the temperature differences.

One of the most used models for piezoelectric films is a strain dependent voltage source in series with a capacitance (except ultrasonic applications). During capacitive load, energy is lost from change to one capacitor to another and very large signals can be created from powerful impacts. During high voltage and frequency, a significant energy loss can occur in form of heat. Silver ink, screen printed into the films, are used to resist high voltage and high localized current. Sensor, which we use (DT1 – 028K) has the same feature, its electrodes are silver in screen printed.

`

2.2.1 Sensor DT1 – 028K [31]

Generally, DT series sensors are available in different sizes and thicknesses. In our experiments, we use DT1-028K piezoelectric film sensor with 28μm thickness. Silver ink screen printed electrodes have protected coatings and lead wires are attached to the rivets. Over 10 millivolts are produces in one micro-strain and capacitance of the sensor is proportional to the area and in oppositely proportional to the thickness. Minimum impedance of the sensor is 1 MΩ and preferred is 10 MΩ and higher. Output voltage of the sensor vires from 10 mV to 100 V, storage temperature from -40°C to +70°C, while operating temperatures are from 0°C to +70°C.

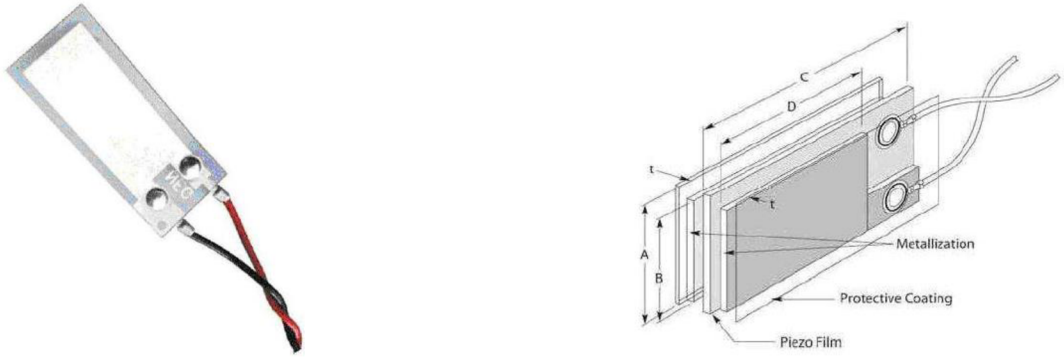

Figure 2-5 PVDF Sensor (DT1 – 028K) - "MSI" [31].

Table 2. Basic Properties of PVDF Film

Symbol	Parameter	PVDF	Units
t	Thickness	28	μm
d_{31}	Piezo Strain Constant	23	x 10^{-12} C/N
d_{33}		-33	x 10^{-12} C/N
g_{31}	Piezo Stress Constant	216	x 10^{-3} Vm/N
g_{33}		-330	x 10^{-3} Vm/N
k_{31}	Electromechanical Coupling Factor	12%	% at 1 KHz
k_t		14%	% at 1 KHz
C	Capacitance	380	pF/cm^2 at 1 KHz
Y	Young's Modulus	2-4	x 10^9 N/m^2
V_0	Speed of Sound	2.2	10^3 in thickness direction

`

2.2.2 Frequency Response and Modes of Operation

Piezo film transducers have a wider dynamic range compared to piezoceramic transducers. As audio transmitters, piezo film vibrates in the length mode (d_{31}). This configuration is used for air ultrasound applications, with a maximum frequency of up to 50KHz. In the case of a high ultrasonic transmitter (>500 kHz), piezo film is in a thickness (d_{33}) mode. Maximum transmission is during thickness resonance. For 28 μm films, the resonance of wavelength is about 40 kHz [26].

$$f_r = \frac{v}{2t} = \frac{2.2\ x\ 10^3 m/sec}{2\ x\ 28\ x\ 10^{-6} m} \approx\ 40\ [kHZ] \tag{16}$$

Resonance values range from low MHz to > 100 MHz for very thin films.

As mentioned above, the piezo film sensor can be operated in two modes: d_{31} mode and d_{33} mode. The first digit shows us the direction of polarization and the second digit indicates how in which direction is stress applied on the film. In the case of "33 mode", stress applies to the surface, in 3 directions, so that the load can be directly on it, the bottom face is fixed. The sensor is compressed, so it acts like a pressure sensor in "33 mode". During "31 mode", stress is longitudinal. In this mode, the side face is fixed, so the stress is in 1 direction [32].

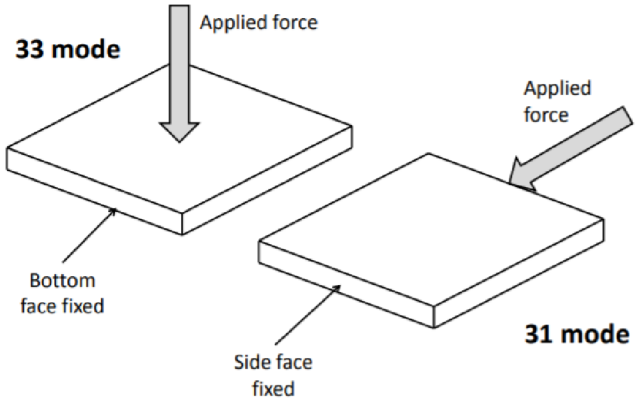

Figure 2-6. Modes of operation [32].

2.3 Piezoelectric Films at Low Frequencies

2.3.1. Capacitance and Equivalent Circuits

One of the main characteristics of the piezo element is its capacitance. Capacitance is the ability to store energy as an electrical charge when to conductive materials are closer to each other. Insulator between these materials has a big influence on the capacitance device. PVDF has a high permittivity, about 12, which is bigger than most polymers. The capacitance of the object is dependent on the area of the material proportionally, a larger

`

area will have higher capacitance. In our case, it is also inversely dependent on the thickness of the film. The formula of the capacitance can be expressed as [26]:

$$C = \varepsilon \frac{A}{t} \,. \tag{17}$$

C - is capacitance of the film,
$\varepsilon = \varepsilon_r \varepsilon_0$, where ε_r – relative permittivity, ε_0 permittivity of free space 8.854 x 10^{-12} F/m
A - overlap area of the electrodes
t – thickness of the film.

Two different equivalent circuits of PVDF sensors can be used. A sensor as a voltage source is in series with PVDF film capacitance, while when it is shunted by internal resistance in parallel PDVF film capacitance – it is a charge source. On the left side of Figure 2-7 you can see a schematic drawing of the voltage source and on the right side, charge source equivalent circuits. V_s is generated voltage from the sensor, proportional to applied stress, Cs is the internal capacitance of the film, V_t is the available voltage at the terminals of the sensor and Q is electrical charge. The open-circuit voltage of the sensor can be calculated as [6][32]:

$$V_v = \frac{Q}{C_s} \,. \tag{18}$$

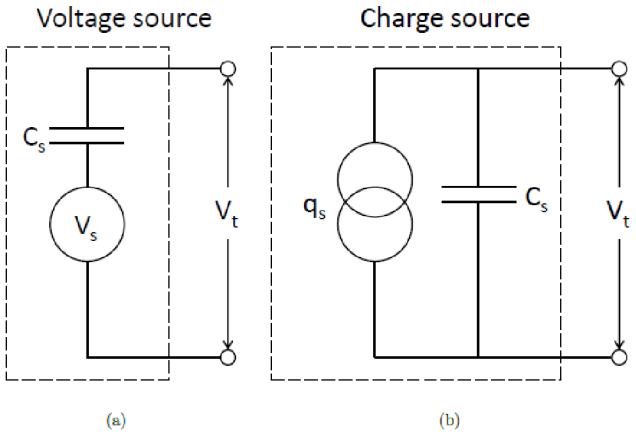

Figure 2-7. Equivalent circuits of the PVDF sensor [31].

2.4 Methods of Cavitation Bubble Generation

There are number of ways to generate and determine behavior of cavitation bubble. In this section, I will review a several methods from different researchers, who have tried and generated cavitation bubbles.

`

2.4.1 Bai et al., [33]

Bai et al., in 2008, made a research about acoustic collapse and rebound of cavitation bubble in deionized water, near a solid wall. They have used VCF1500 ultrasonic processor in order to create high power ultrasound, with a frequency of 20 kHz. High speed camera, Photron Fastcam SA-1 and MotionXtra HG-LE, with the help of the xenon flash lamp were used to capture cavitation bubbles. Framing rate was 1 x 10^5 fps. At first, as a higher frame rate was necessary, they were not able to capture clear quality pictures, so that it was not able to have information on bubble surface from these pictures on the Figure 2-8.

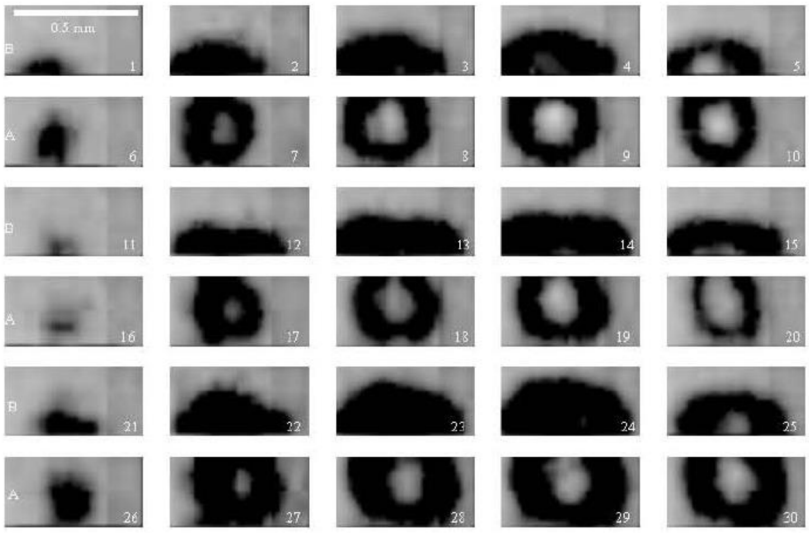

Figure 2-8. Collapse and rebound of cavitation bubble [33].

In Figure 2-9, you can see the cavitation microjet. After the first collapse, bubble is divided into two small bubbles. It is common for acoustic cavitation bubbles. Mostly, during when positive acoustic pressure is positive, these two small bubbles collapse in the direction towards each other. If the acoustic pressure is negative, they can rebound and create one bubble.

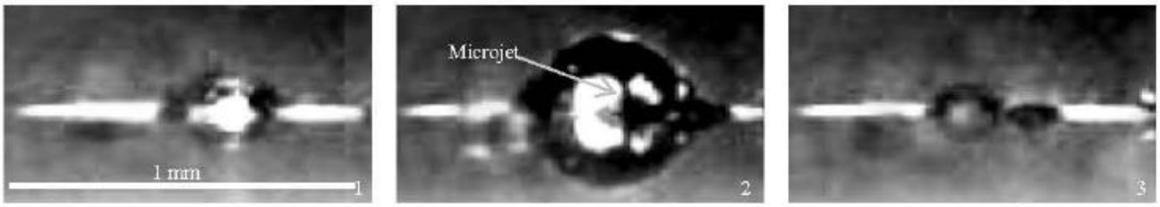

Figure 2-9. Cavitation microjet [33].

From above mentioned and other experiments conducted by the authors, they concluded that cavitation bubbles are consistent with acoustic cycles. Deformation of the bubble had happened in two acoustic cycles, the spherical bubble collapses towards to boundary and rebounds and grows again as a toroidal bubble, after that it collapses again towards the center of its minimum volume and then rebounds again.

`

2.4.2 Shan et al., [34]

Another method of the generation of cavitation bubble is underwater pulsed discharge. Shan et al., in 2018, made an experiment using this method, to investigate energy efficiency cavitation bubble inducing, characteristic of the discharge with different properties and profile of the cavitation bubble itself. This method is very actively used in recent years, because it makes possible to observe various different phenomena happening in this field. In this experiment, cavitation bubble is induced by high DC voltage from a Walton voltage multiplying rectifier module, high-speed camera (AcutEye-3M-540CXP) at the frame rate of 34500fps is and pixel resolution 128x128 is used to capture processes. A digital oscilloscope (Tekronix DPO3034) was used to detect the waveforms of current and voltage. Other equipment used are: discharge switcher, capacitor bank, water tank and electrodes.

Applied voltage for this experiment was 10.2 kV and needle-needle tungsten electrodes were used to make discharge. From the pictures in Figure 2-10 it is visible that the bubble has almost a standard sphere shape and a maximum diameter of the bubble is 9.3 mm. 1043μs was needed form the generation to the collapse of the bubble.

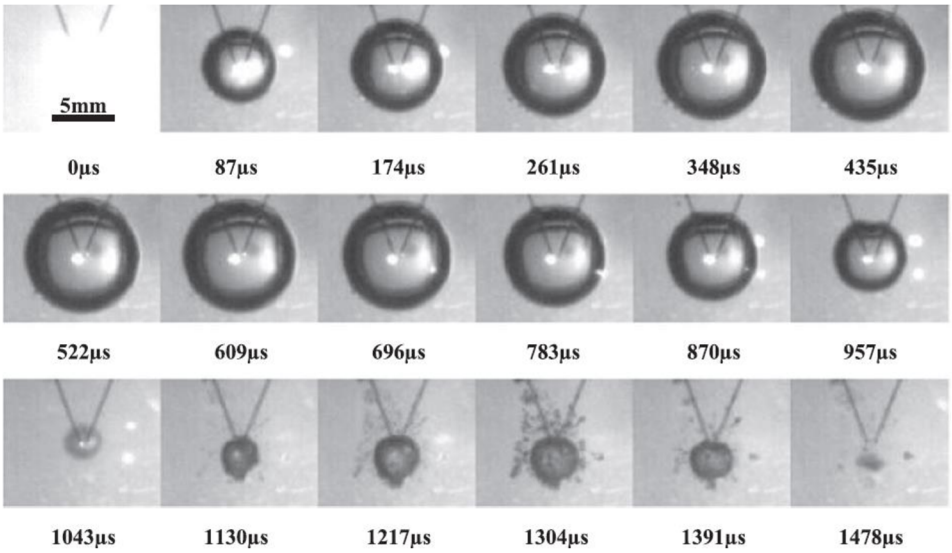

Figure 2-10. Evaluation of cavitation bubble[34].

Authors have found that higher voltage results in a short pre-discharge phase. Also, that the voltage is decreasing having a certain slope in pre-discharge phase. During the high voltage discharge, the dielectric breakdown of the water happens between the electrodes, resulting to an induced cavitation bubble by liquid vaporization. Deposited energy is expressed as an integral of instantaneous power in the discharge phase:

$$E_d = \int u_i i_i dt \ . \tag{19}$$

Where, u_i and i_i are instantaneous voltage and current.

From the experiments, authors conducted, they found that bubble energy distribution has some dispersions. This may be caused by the instability of the pulsed discharger, caused by

`

the thinner electrodes and small gaps between them. The smaller gaps mean bigger sensitivity on the distance and thinner needles can easily cause distance variety because of the mechanical shock discharging [34].

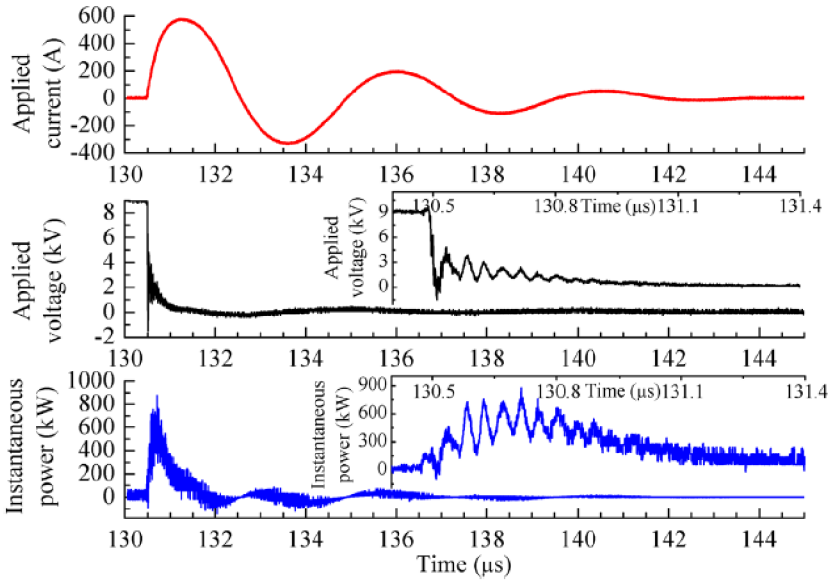

Figure 2-11. Waveforms of applied voltage, current, and instantaneous power [34].

Underwater pulsed discharger has some advantages, it is simple, portable and easy to use. Here, I would like to mention that, I will also use not exact but similar method in order to investigate cavitation bubble dynamics. Experimental setup, pictures of bubble generation and collapse patterns, with all the data acquired will be discussed further.

2.4.3 Schovanec et al., [35]

Schovanec et al., in 2019, made experiments on laser-generated plasma, followed by shock waves and increasing cavitation bubbles in order to observe the velocity of the shock wave after the initial cavitation bubble. Laser induced breakdown (LIB) method was used. It is a method to generate single cavitation bubble, which will have certain position in a volume, inside the glass tube. Not only cavitation bubble, but also a natural plasma is generated by LIB. In the experiment, authors used two lasers, one of them was serving generation of plasma shock wave and bubbles and the second one used to illuminate glass tube in order to take good quality photos with high-speed CCD camera, function generator, was used to synchronize lasers and camera. Pulse of the laser Nd: YAG New Wave Solo III PIV was t=6 ns and wavelength λ=532 nm. Shadowgraph setup was used for the visualization of the shock waves, this means that except lasers and camera with a microscope, there also were DCM dye and optical filter. Resolution of the camera was set as (640 x 480) pixels, dynamic range 12-bit, exposure time was two times 100 ns with a 100 ns time break.

`

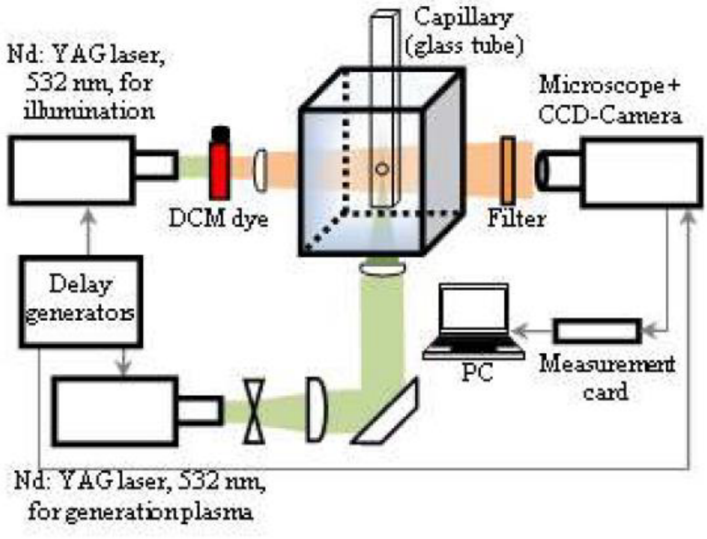

Figure 2-12. Experimental setup [35].

In time frame t_1 we can see generation of the bubble and its shock wave. Shock wave in this experiment, is captured in time 700 ns, and it continues for 500 ns and after that it is reflected and moves towards the bubble. In larger tubes, shock wave reflections occur later and in a smaller tube pressure is greater.

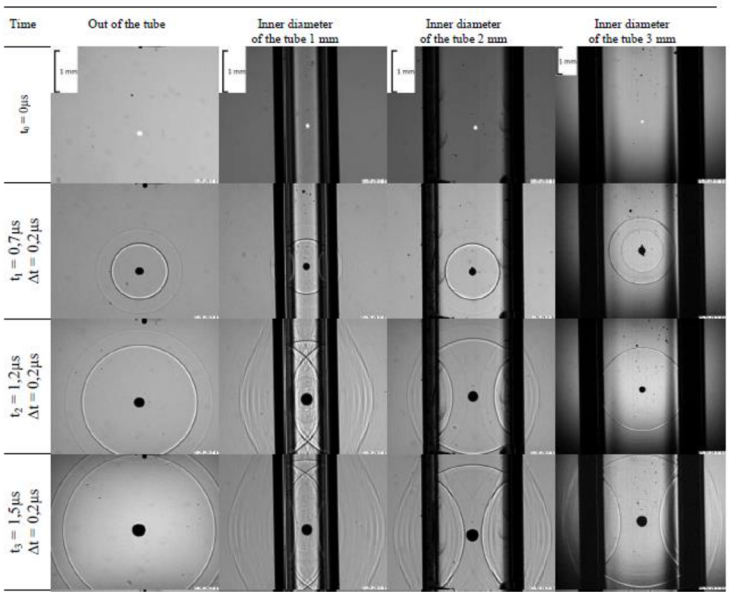

Figure 2-13. Evolution of the shock waves from the experiment [35].

After several experiments in different tubes, authors compared behavior and velocity of the shock waves. Speed of the shock wave in the micro-capillary is higher and in cuvette, because of the pressure increase in a smaller place, and also because that shock wave velocity also depends on tube diameter, however it is still not clear, if vapor bubble appears due to the pressure decrease from the evaporation in the liquid or from the leakage of the cavitation bubble.

`

2.5 Wang and Chen [36]

In 2007, Wang and Chen made a number of experiments in order to detect and investigate impulsive forces, cause by collapse of cavitation bubble near a solid boundary. They've used already above mentioned 28 μm PVDF sensor (DT1-028 K/L, Measurement Specialties) Sensor was calibrated with a pendulum type ball impact technique and bandwidth of the frequency of piezoelectric film was determined by a gas dynamic shock tube.

Plasma, formed by the released energy from the cavitation bubble, leads to initial breakdown. Shock wave is created because of this. After the initial breakdown, collapse and rebound cycles happen, in which pressure pulse is captured practically at the instant of minimum bubble volume. When bubble collapse is near to a solid wall, reentrant jet forms, which impacts the other side surface of the bubble divides it into many pieces. If the process is far from boundary, jet impact results only in one or two toroidal bubbles. On the Figure 2-14a you can see pressure variation nearby the bubble and on the Figure 2-14b is variation of the bubble radius with time.

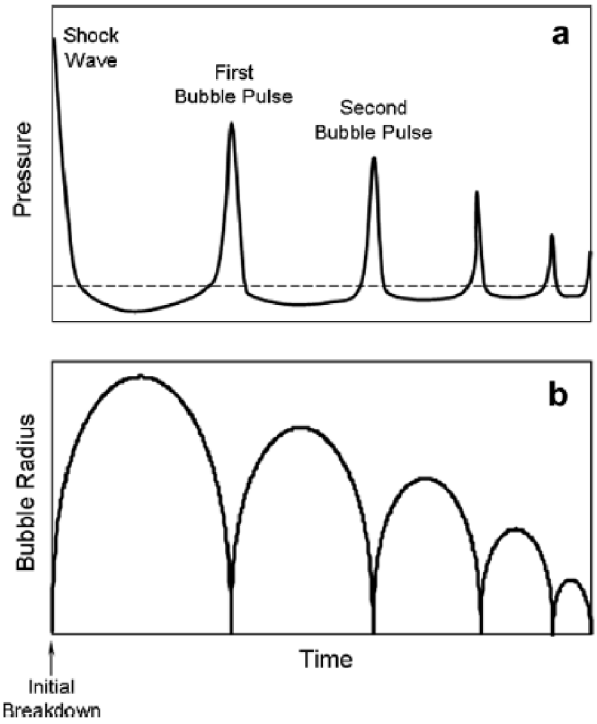

Figure 2-14. Dynamics of a spherical bubble generated by deposition of energy [36].

Important parameter, which has significant effect on the three mechanisms (shock wave, microjet and splash) happening during and after bubble collapse, is the ratio "γ". This is distance bubble created from the boundary over a maximum bubble size ($\gamma = L/R_{max}$) In this study, authors, used different values γ, specifically from 0.14 to 8.

`

Experimental setup includes discharging capacitors, tungsten electrodes, 10 kV electrohydraulic charge generator. Received signals are then digitized by an oscilloscope (TDS3032) and captured by a high-speed CCD camera (Kodak, SR-Ultra).

In Figure 2-15, when the ratio of $\gamma = 2.85$, it is clearly visible that the bubble reaches maximum radius at the 12^{th} frame, so the pressure inside the bubble is much lower than ambient pressure, this is the beginning of the bubble collapse. Shape of the bubble collapse is also dependent on the distance from the boundary. It is visible in this example that, even the collapse is spherical until the final stage, after which bubble collapse instantaneously (frames 20-22) and creates rebound and the shockwave is generated. On frames 23-28 high-speed microjet is visible and the protrusion is shown on the lower part of the bubble.

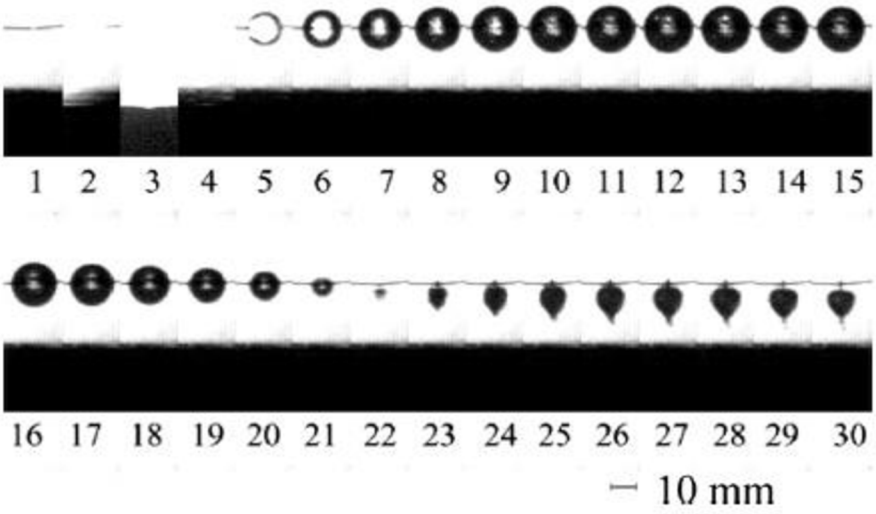

Figure 2-15. Cavitation bubble collapse near a solid boundary.
$\gamma = 2.85$. (interval-100 μs, 10000 fps) [36].

As I've mentioned before, Wang and Chen made experiments several on several distances, I won't discuss each of them, but will talk about the conclusions they've made. Firstly, if $\gamma \geq 3$, bubble period is practically two times bigger than Rayleigh collapse time, the first collapse is spherical and only about 13% of bubble energy is remained after it, mostly the energy lost is transformed into a shock wave.

During $1.1 < \gamma < 2$, the closeness of the boundary is the reason of the bubble collapse. The result caused by microjet effect is that the first bubble period is increased notably, maximum impact force and bubble impulse are slowed down by decreasing of γ, while, the energy of the collapse of the second bubble increases significantly.

For the $0.6 < \gamma < 1.1$, peak impact force decreases instantly from $\gamma = 1.1$ to a minimum at $\gamma = 0.9$ and then recovers back. In the meantime, first bubble period increases to a maximum. The force initiated by the jet on the wall is small. Splash effects are captured before the bubble is compressed to its minimum volume and the strength of it decreases together with γ, until $\gamma = 0.6$, in this time, splash disappears. For $\gamma = 0.6$, multiple shock waves are recorded instead of a single pulse. More than 4/5 of bubble energy is released at the first collapse and because of this, peak impact force and the bubble impulse are one order of magnitude larger, than at the second collapse of the bubble.

`

3. METHODOLOGY

This chapter represents the methodology of the practical part of this master's thesis. As mentioned above, aim of this work is to try and separate individual impacts of the cavitation shock wave and microjet, received from the signal near a solid boundary. In our case, 2 PVDF sensors are used for the experiment. Bubbles are generated by electrical charge, under the water, in an experimental tank sized 450 x 250 x 300 mm. This method, is similar to the method, used by Wang and Chen [36] but is has some differences, first of all usage of the second PVDF sensor. This chapter also includes information, about the equipment used during experimental work, setup of them, as well as, information about used PVDF sensors, their fabrication, calibration and post processing of the signals received from these sensors.

3.1 Equipment Used

This chapter describes the information about the common devices used during the experiment, their properties and parameters. Secondary equipment, such as camera tripod, stand and etc. are not described in detail.

Tektronix AFG 3102 – Arbitrary/Function Generator

Tektronix AFG 3102 is dual-channel function, arbitrary waveform and pulse signal generator. It can generate not only standard function waveforms such as sine (user can choose between 12 standard waveforms), with different amplitudes (10 MHz, 25 MHz, 100MHz), but also arbitrary waveforms with up to 128 K in length (14 bits, 250 MS/s, 1 GS/s or 2 GS/s). For user-defined pulses, the frequency can be set from 1mHz to 50 MHz, with the amplitude of 20 mV_{p-p} to 10 V_{p-p} for 50 Ω load and 40 mV_{p-p} to 20 V_{p-p} for open circuit ($_{p-p}$ means range between peaks). The device has 2 output channels, one auxiliary input, one auxiliary output and the trigger.

Figure 3-1. Signal generator.

`

Programmable Power Supply – GW INSTEK PST-3202

GW INSTEK PST-3202 is a programmable linear DC power supply, with 3 channels of voltage outputs. Two of this three outputs have voltage range from 0-32 V and current - 0-2 A, while the third one has 0-6 V and 0-5 A. Device have, over-voltage (OVP), overcurrent (OCP), overtemperature (OTP) protections. Resolution voltage is 10 mV and resolution current 1mA. For the voltage, accuracy of the device is $\leq 0.05\% + 20$ mV and for current it's $\leq 0.1\% + 5$ mA. For our experiments, we use this device as a source of constant voltage (25 V), but it has to be mentioned that it can work as a source of constant current. All outputs are shown simultaneously on the LCD display of the device.

Figure 3-2. DC power supply.

NI PXI-1033 chassis with NI PXI-5105 Oscilloscope

NI PXI-1033 is 5 slot chassis that is used in for a lot of PXI applications in different industries. It has 3U PXI and CompactPCI modules, an integrated controller, auto/high temperature-controlled fan. PXI stands for PCI eXtensions for Instrumentation, they are used as a basis for a lot of electronic test devices, automation systems and etc. They are based on standard computer busses, which allow more flexibilities in equipment. NI PXI-1033 can be used to have a remote connection between the chassis and a PC. 2 slots are used in our equipment, one is used with NI PXI-6711 analogue output (which is not used by us) and the second slot is for 12bit NI PXI-5105 Oscilloscopic card, which is interesting for us.

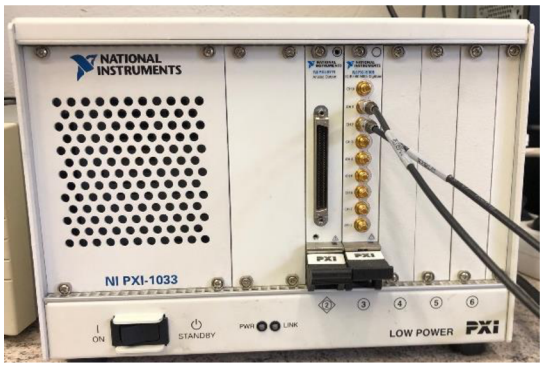

Figure 3-3. NI PXI chassis with oscilloscope.

`

This module is built up with electrical circuits of an oscilloscope, but the final signal is processed by the computer. It has 8 channels, with settings for voltage range, filtering, impedance and coupling. Input impedance values are 50 Ω (input coupling – DC) or 1 MΩ (input coupling – AC, DC). Input voltage values can be: 0.05 V, 0.2 V, 1 V and 6 V for 50 Ω and1 MΩ and in case of only 1 MΩ – 30 V. The maximum time base frequency is 60 MHz. The device is connected to the computer via a NI ExpressCard 8360.

CCD Camera – NanoSense MKIII

In our experiment, we use a high-speed charged-coupled device (CCD) camera Nanosense MKIII with the maximum resolution of 1028 x 1024 pixels at 1000 fps. Sample frame rates are depending on the vertical resolution and they increase as the resolution is decreased. For example, a maximum of 64 000 fps, is reached during a vertical resolution of 16 pixels, that's why it is suitable for our experiments. The device is acquired with Nikon AF Micro-Nikkor 60 mm f/2.8 D optical lens, with parameters: focal length 60mm, maximum aperture number-32, angle of view 39.6, luminosity – 2.8 and shortest focusing distance – 0.22 (at 1:1 scale). The camera is connected to the signal generator Tektronix AFG 3102 via BNC connectors and trigger is used to start the capturing. Special software Motion Studio is used to control the camera from the computer. For the purposes of our experiment, the camera is mounted on the tripod.

Figure 3-4. NanoSense MKIII.

To scan and capture the cavitation bubble and its collapse properly, it was necessary to use additional lighting. For this reason, high power LED light, with a luminous flux of 1000 lm was placed on the second side of the water tank and light was positioned in the direction of the camera, additionally, the lens was inserted between the light and the camera in order to focus the light in the needed direction.

Figure 3-5. LED Lighting.

`

3.2 Steel Plate with PDVF Sensor

For the experiments, two steel plates, with dimensions 80 x 10 x 50 mm were used as a solid boundary and PVDF Sensors DT1-028 K/L were attached to them. The plate can be grounded, from the holes for screws, located on the corners of the plate. Initially, a metal rod was used to fix plates at necessary distances, but then, due to disturbances in the signal, a plastic rod was used instead of metal, more information about this, will be discussed in the next chapter. The steel plate was treated and cleaned using two types of sandpaper, after which isopropyl alcohol was used for further cleaning. Henkel Loctite Super Bond glue was applied to the surface of the plate, distributed very carefully and evenly, as a thin layer, on the necessary area of a plate and after which PVDF sensor was placed and glued on it.

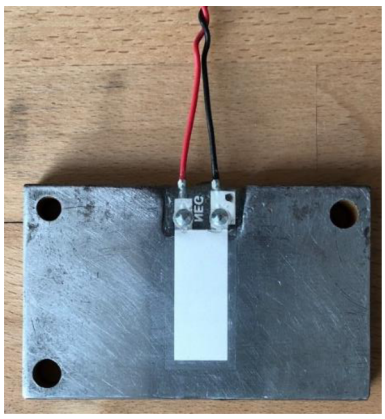

Figure 3-6 PVDF sensor on a steel plate
(without adhesive tape)

For additional safety and protection, an adhesive tape was applied on the sensor. In order to minimize the risk disturbance from the plate, remaining free spaces, as well as the silver inked electrodes, and lead wires with rivets were filled and glued using two-component, waterproof and transparent epoxy adhesive glue – “Bison Epoxy 5 Minutes”.

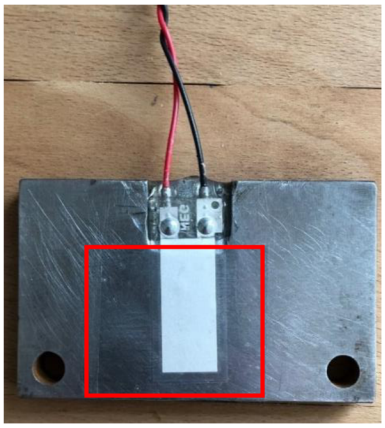

Figure 3-7. PVDF sensor on steel plate
(with adhesive tape)

`

3.2.1 Sensor Calibration

As it's known, the PVDF sensor's output signal is measured as voltage, which is proportional to the force or the pressure acting on the surface of the film. Nowadays, 3 most common methods: the ball drop method, a pendulum-typed ball impact and lead breaking method are used to calibrate PVDF film sensors [37]. For this work, the ball drop method was used. During this method, a stainless-steel ball is dropped in the glass tube, from the initial height of h_1, after hitting transducer, rebounds to height h_2. Schematically, it is shown in Figure 3-8**.** Since the rebound is very fast, slow-motion camera and ruler is used to capture the exact height of the rebound. Electric charge, generated by the ball drop, can be measured as maximum voltage V_{max} and as a time duration of the impact τ using a DAQ, in the LabVIEW Signal Express Software. Calibration signal of the $m = 1.250\ g$ ball and the initial starting position is shown in Figure 3-9.

Determination of mean impact force is based on the impulse-momentum theorem and can be calculated as [37]:

$$F_{mean} = \frac{1}{\tau}\int_{t_1}^{t_2} F(t)dt \ = \frac{m}{\tau}\ (v_1 + v_2)\ . \tag{20}$$

Where, τ is impact duration time, v_1 is velocity just before the rebound, v_2 is just after the rebound. The ball is dropped from the initial position is h_1 and rebounds to the second position - h_2. Velocities can be calculated using formula:

$$v_{1,2} = \sqrt{2gh_{1,2}}\ . \tag{21}$$

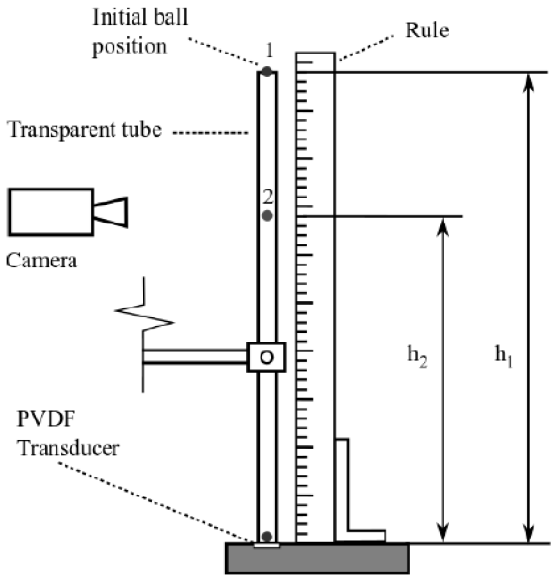

Figure 3-8. Ball drop method [37]

`

Maximum force can be considered as two times mean force:

$$F_{max} = 2 \cdot F_{mean} \tag{22}$$

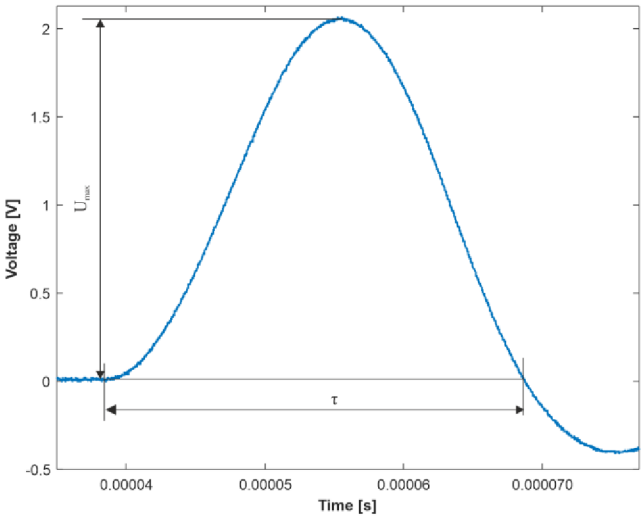

Figure 3-9. Calibration signal from 1.250 g. ball drop.

3.3 Experimental Setup

The aim of this work is to try and distinguish two cavitation phenomena, shock wave and microjet from the received signal. For this reason, a method of generating cavitation bubbles by underwater electric discharge was chosen in this thesis. Many researchers, such are: Wang and Chen, Shan et al., used this type of approach to study cavitation bubble dynamics. Experimental setup in this research is like this: 2 PVDF sensors, glued on the stainless-steel plate was placed in different distances from each other, in order to try force and pressure effects closer and far from bubble generation and its collapse. CCD Camera in active mode for the whole measurement to film the activity of cavitation bubbles, experimental setup can be seen in Figure 3-10. Bubbles are created by two needle-needle electrodes, connected to the capacitor, in order to supply electrodes. The capacitor has its own switch, turning it on provides a charge of the capacitor bank itself from the DC Voltage Gwinstek PST-3202. In Figure 3-11 you can see, supporting structure, designed especially for this experiment.

`

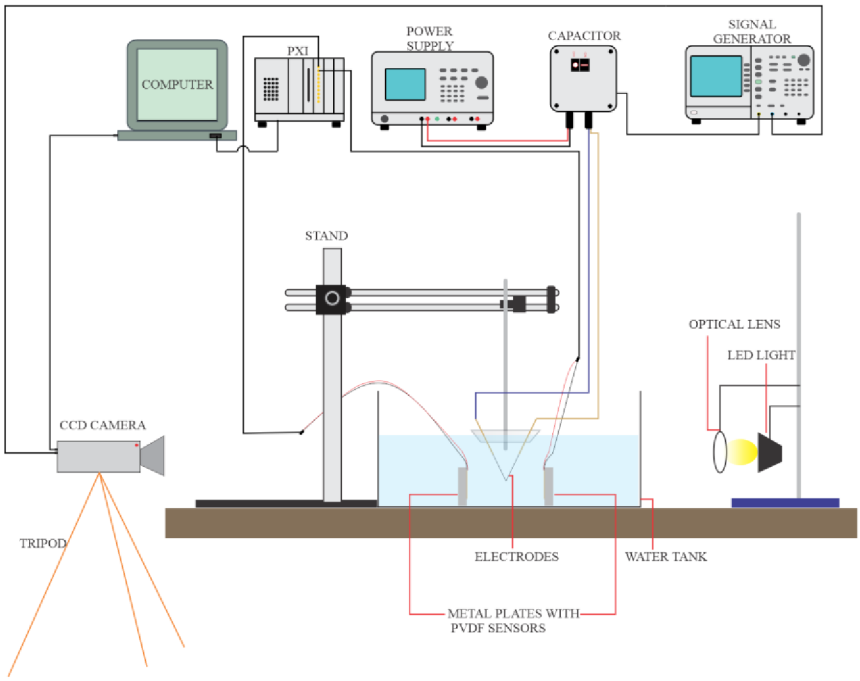

Figure 3-10. Experimental setup.

The supporting device is made of the poly (methyl methacrylate) PMMA material, also known as plexiglass. In the middle, it is threaded and steel rod is fixed on it with screws. Holes for the electrodes are drilled diagonally, also fixed with the locking screws, preventing electrodes to slide. Electrodes are made from copper; the diameter of bigger electrode is 3 mm and for smaller is 0.05 mm. Thinner conductor is attached to stronger one for the supporting reasons.

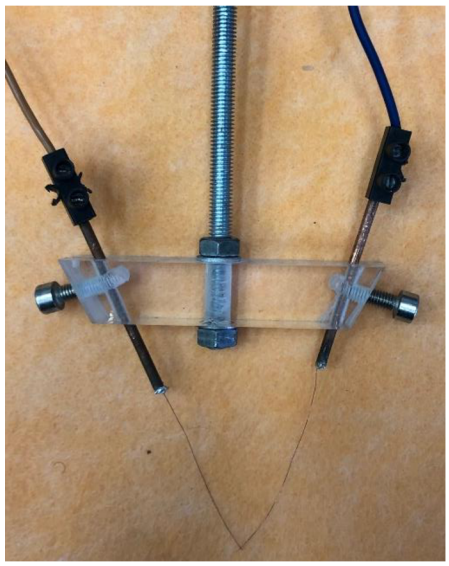

Figure 3-11. Supporting structure.

The first step to begin an experiment is to charge capacitor from the DC power supply. CCD camera, PXI box and capacitor relay are all connected to the signal generator. The signal applied to the relay, switches the circuit, while also a signal from the function generator is

`

needed to start the camera. After pressing the trigger of the signal generator, a bubble is created at the contact point of electrodes. With the camera, it is visible that the bubble goes through its life cycle, happening with phenomena such are jet effect and splash. PVDF film captures one combined signal from all of these effects, transmitting it directly to the PXI oscilloscope, from which it is sent to the Signal Express software, on PC.

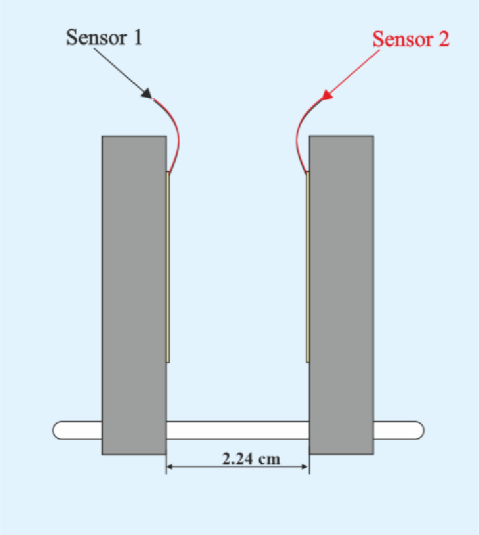

Figure 3-12. Installation of sensors.

3.4 Signal Processing

Signal from a PVDF sensor is received by the NI PXI-5105 Oscilloscope and then it is processed in the NI Signal Express software. As mentioned, two PVDF sensors are used for this work, both of them calibrated and used to capture signal from bubble generation, its collapse and other processes during this phenomenon. Results of the calibration can be seen in Appendix (Table A1.) DAQ settings are set as following:

- Voltage Range – 5 V
- Offset – 0 V
- Channel 1 (for Sensor - 1)
- Channel 2 (for Sensor - 2)
- Coupling – DC
- Input Impedance – 1 MΩ
- Sample Rate (S/s) - 60 M
- Record Length – 100000
- Bandwidth – 0 Hz
- Trigger type – Edge
- Source – Channel 1 (for Sensor – 1), Channel 2 (for Sensor – 2)
- Ref Position – 0
- Level (V) – 0
- Slope – Positive
- Max time (s) - 15 s
- Delay (s) – 5 s

`

Received signals from Signal Express can be exported in .xlsx, .txt, .lvm and other formats.

Calibration was made using the ball drop method. The length of the tube used for the ball drop was 400 mm, area of the PVDF sensor was 12 mm x 30 mm. The horizontal axis in the received signal represents the time and the vertical axis - voltage. Below are shown the signal results received from the drop of 4 different weight steel balls.

In Figure 3-13, signals are shown from both PDVF sensors, after dropping the ball, with a mass of $m = 0.438\ g$. The average maximum voltage received is $V_{max} = 1.18\ V$. Average time duration of the impact is $\tau = 24\ \mu s$, with a minimum time duration of 23 μs and a maximum time of 25 μs.

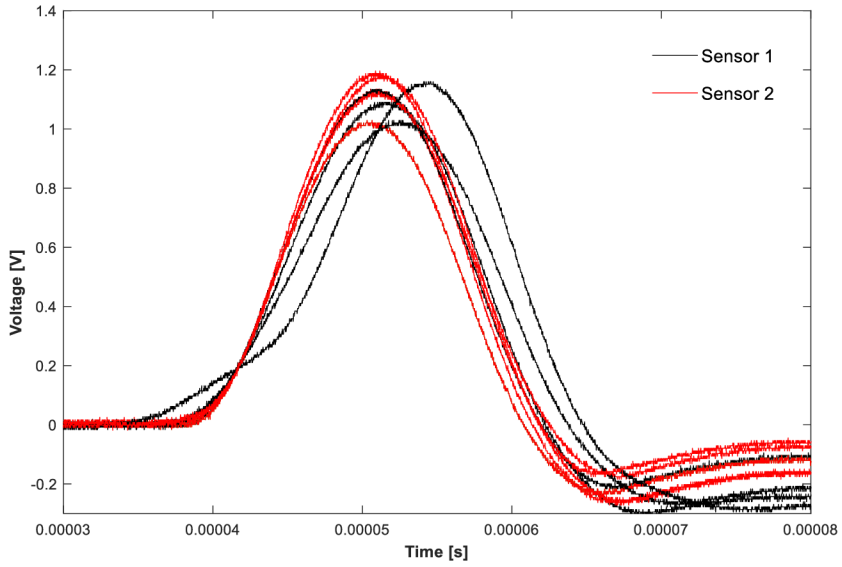

Figure 3-13. Calibration signal from both sensors (Ball – 0.438g).

PDVF Sensor – 1 and PVDF Sensor – 2 were placed facing each other, while, electrodes placed between them, creating an electrical spark and the following signal was captured using these sensors. Experiments were conducted for a different range of proximity parameter γ, which is the ratio between the distance from the surface to the bubble center, over a maximum radius of the bubble ($\gamma = R_1/R_{max}$). Below are placed figures, just for visualization of some main parameters of the signal. Received signals will be discussed in the details in the next chapter.

In Figure 3-14 there are signals, received from the two PVDF sensors, placed 2.24 cm from each other and bubble generation is happening 1 cm far from the sensor – 1. Maximum bubble radius $R_{max} = 5\ mm$, therefore parameter $\gamma = 2.0$. It is clearly visible that, the voltage amplitudes of the bubble collapse signal (hence the force, since we know calibration results between voltage and force) are significantly bigger for the closer sensor, which is not surprising. Here, the maximum voltage captured by the first collapse of the bubble reaches the amplitude of $V_{max} = 4.9\ V$.

`

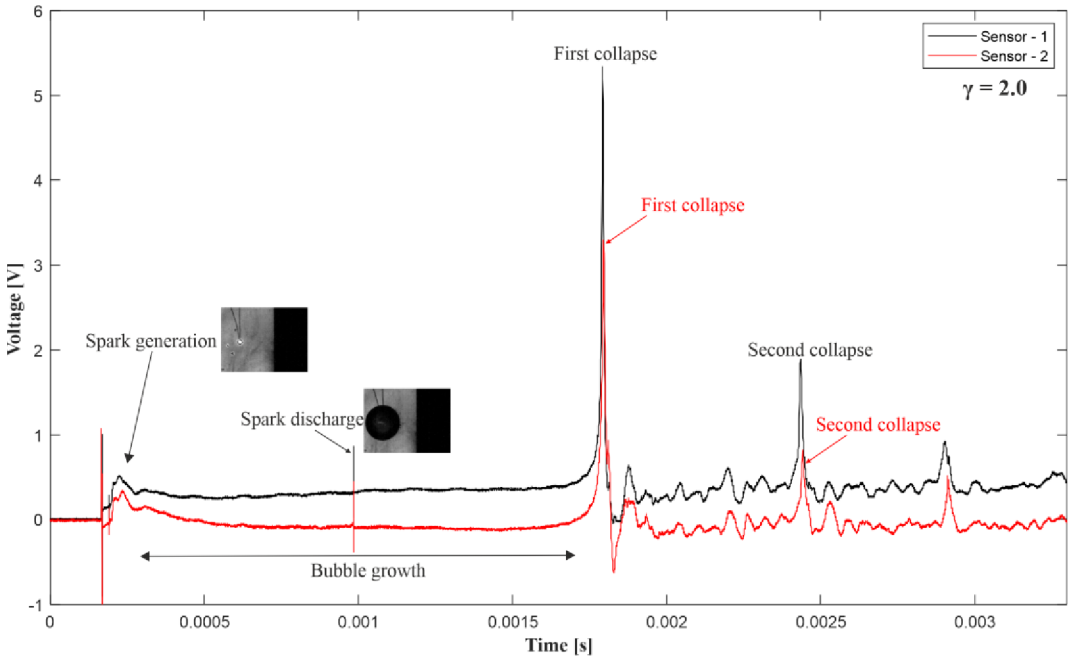

Figure 3-14. Typical signal from spark generation and bubble collapse

4. RESULTS AND ANALYSIS

This chapter includes results obtained from the calibration of the different PVDF sensors, signals received due to the collapse of the cavitation bubbles. The setup includes two metal plates, with one sensor placed on each, connected with a plastic threaded rod. The idea of two sensors is based on the sound or shock wave propagation and inverse square law. It will be further described.

4.1 Problems Occurred During Experiment

Before I start the review of the results, I would like to briefly talk about the problems that occurred during the experiment. For this research, a lot of different variations and setups of PVDF sensors were used. Firstly, in the early stages when I tried to examine the bubble collapse phenomenon, two metal plates were connected via the threaded steel rod. The problem, in this case, was, that despite the usage of the groundings in different places to receive the correct signal, results were not satisfying, because there still were some fluctuations and disturbances in the received signal. To resolve this problem, a plastic threaded rod was used and it had a notable effect. Another problem, which may have an impact on the receiving signals, is gluing. In order to receive the correct signal, rivets of the PVDF sensor must be isolated from the metal plate, which can be achieved by gluing. Additionally, despite the isolation between metal plates, also silver ink electrodes have to be well glued to prevent water leakage between glue and electrodes because it also has a significant effect on the receiving signal. On both of the sensors, the protective layer of the

`

tape was used before the experiments and calibration, because close impact can damage plastic cover of the sensor.

4.2 Calibration Results

in Figure 4-1 (a) and (b) calibration results of sensor - 1 and sensor - 2 are shown. Maximum voltage and maximum impact force are compare plotted in these charts, showing linear increase relation between them. The linear least-squares method was used for the calculation of the sensitivity constant. The sensitivity constant received from the calibration and linear least-squares method for first PVDF sensor is $V = 0.0051\ F\ [N] + 0.2534$, fitting line value $R^2 = 0.9852$, while for the second one, $V = 0.005\ F\ [N] + 0.2862$ and $R^2 = 0.9747$ respectively.

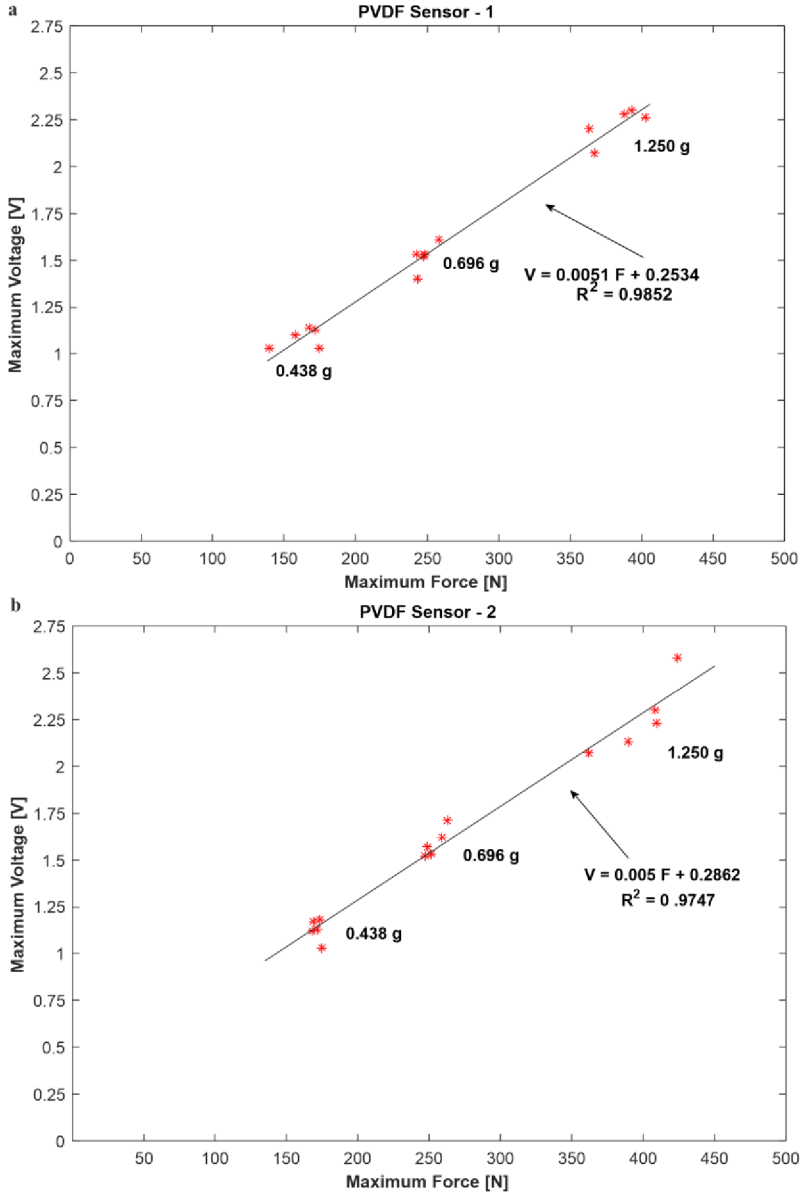

Figure 4-1. Calibration curve for PVDF sensors.

`

4.3 Experimental Results (The Model of the Inverse Square Law)

As it was mentioned before, for this experimental work was decided to use the setup with 2 PVDF sensors fixed on a two steel plates. At the beginning of the work, it was not known to us if this setup would give satisfactory results, because measuring the exact impact of cavitation microjet is quite complicated and a lot of authors had problems with it. In most cases, cavitation microjet has no significant effect in the case of amplitude and it can't be measured properly. Since we work with shockwaves, the first model used to measure load impacts is dependent on inverse square law. Generally, inverse square law applies to quantities that are inversely proportional to the square radius (or distance) from the source. This can be applied to the intensity of the shock wave. In the case of spherical waves, intensity (or energy) reduces inversely squared from the center of the wave source. Considering this, the intensity of the shock wave will be:

$$I = \frac{P}{A} = \frac{P}{4\pi r^2} . \tag{23}$$

Where, A is the surface area of the sphere. So, $I \propto 1/r^2$ ($\propto$ - proportional). In acoustics, wave pressure is decreasing not inverse squarely but inverse proportionally, it means that pressure decreases inverse proportionally to the distance, so: $P \propto 1/r$. Since pressure measuring device is not used in this experiment, we will use this relation in this chapter. As it is mentioned in the technical manual [26] of the piezo film sensors, in the mode g_{33} (when a force acts to compress the film's thickness) it's possible to measure applied stress on the sensor.

$$V_0 = -g_{33} \cdot X \cdot t_f \tag{24}$$

Where, g_{33} is piezo stress constant [Vm/N], X is applied stress (pressure) in [N/m^2] or [Pa] and t_f is PVDF film thickness [μm]. In this case $g_{33} = 330 \cdot 10^{-3}$ V·m/N, t_f = 28 μm.

As it was already said before, the PVDF sensor recognizes signals in voltages and with a proper calibration constant, this voltage can be converted into force. At first, to check if this model was appropriate, shock wave signal was measured practically exactly in the middle of two sensors, with proximity parameter γ = 3.35 (ratio between the distance from the wall and maximum bubble radius) to be sure that wall doesn't affect the bubble and there wouldn't be any other process than shock wave so that the signal on both sensors would be the same.

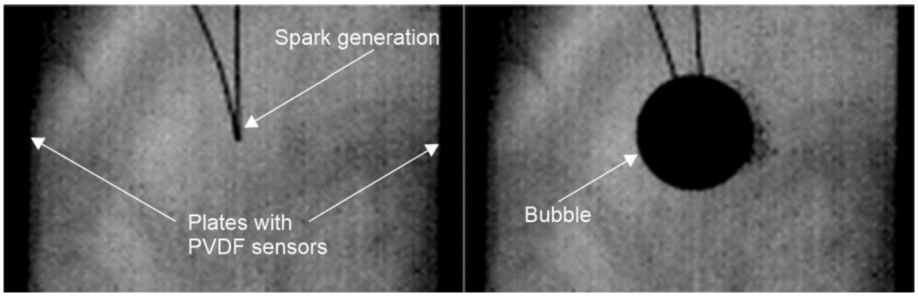

Figure 4-2. Bubble generation in the middle of sensors.

`

In the Figure 4-2, you can see the location of the electrodes for spark generation and bubble during its maximum radius. Truly, signals received from sensors are practically identical (an only minor difference which is acceptable and predictable, because electrodes are located 2mm closer to one side, distance from the right sensor is 11.1mm and from left 11.3 mm). The maximum voltage recorded by the first sensor is $V_{1max} = 1.44\ V$ and by second $V_{2max} = 1.48\ V$ respectively.

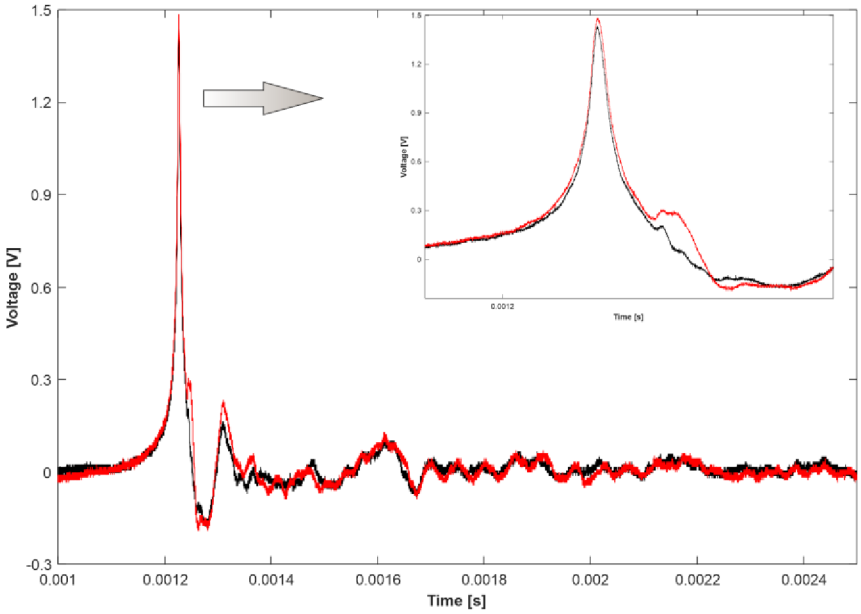

Figure 4-3 Signals received (bubble in the middle)

Based on the equation (23) stress on 1st sensor is equal to $P_1 = 154.7\ kPa$ and on 2nd it is equal to $P_2 = 160.1\ kPa$. Based the model of inverse distance,

$$\frac{P_2}{P_1} = \frac{r_1}{r_2} \tag{25}$$

If we take radius r_2 as a reference, in ideal case, pressure on the first sensor, should be equal to

$$P_1 = P_2 \frac{r_2}{r_1} = 163\ [kPa] \tag{26}$$

Values from the model and calculation are in a close and acceptable range. Furthermore, if we calculate forces using calibration sensitivity constant, the maximum force acted on the sensors are $F_{1max} = 232.6\ N$ and $F_{2max} = 238.7\ N$ while in an ideal case, model force on the first sensor should be $F_{max} = 243\ N$. These minor differences are caused based on different reasons, such are different calibration sensitivity of each sensor, also the source of the shock wave is not in the exact, perfect center, but some small (2mm) difference. In Figure 4-4 (a) and (b) you can see the theoretical and experimental values of forces and pressures during first collapse of the bubble (for different distances from the wall - different values of γ). As it is visible from the charts, during < 1, there are big differences between model and actual pressures and forces, while it is practically very close $\gamma \geq 1.3$. It is not surprising, because when a bubble is too close to the wall its shape is not spherical, it is defected. Also, in close range microjet can occur even during the first collapse and furthermore the law can't be

`

properly used for second-growth and collapse of the bubble, therefore can't be used to detect the impact of microjet caused by secondary impacts.

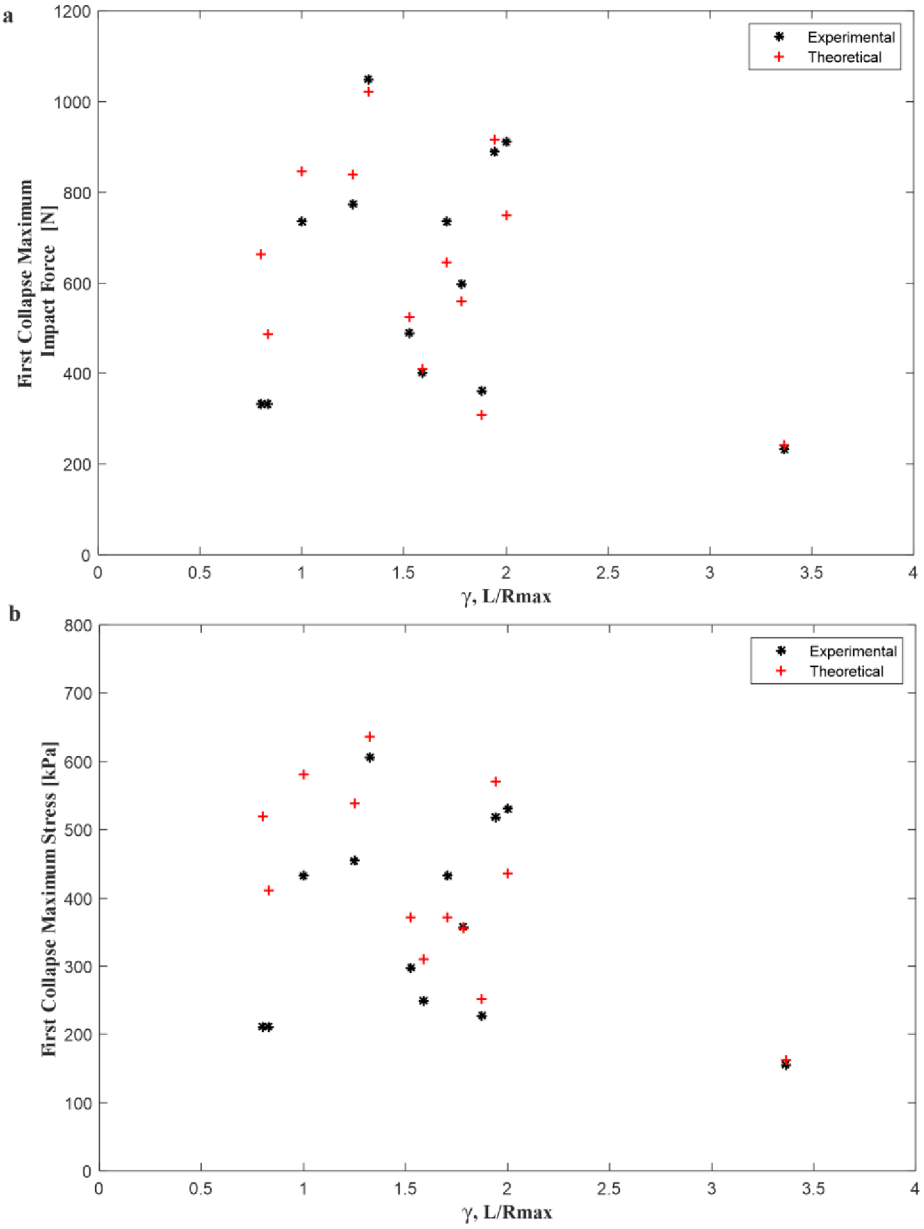

Figure 4-4. Theoretical vs experimental impacts on sensors.

4.4 Impact of Bubble collapse near the wall

Electrical spark discharge is one of the most common method to create small cavitation bubbles underwater. In this part of the thesis, cavitation bubble behavior near the solid boundary is described. In this case, solid boundary is the metal plate on which PVDF sensor is fixed. The characteristics of the bubble is dependent on the distance of the bubble from the wall *L [mm]* and also on maximum bubble radius R_{max} *[mm].* Proximity parameter also called stand-off distance, γ is the ratio of between these two variables:

`

$$\gamma = \frac{L}{R_{max}} . \tag{27}$$

The size of the bubble is dependent on the voltage applied to the electrodes. For this research 25 V were used. Figure 4-5 represents first cycle times (from generation to first collapse) of different sized bubbles.

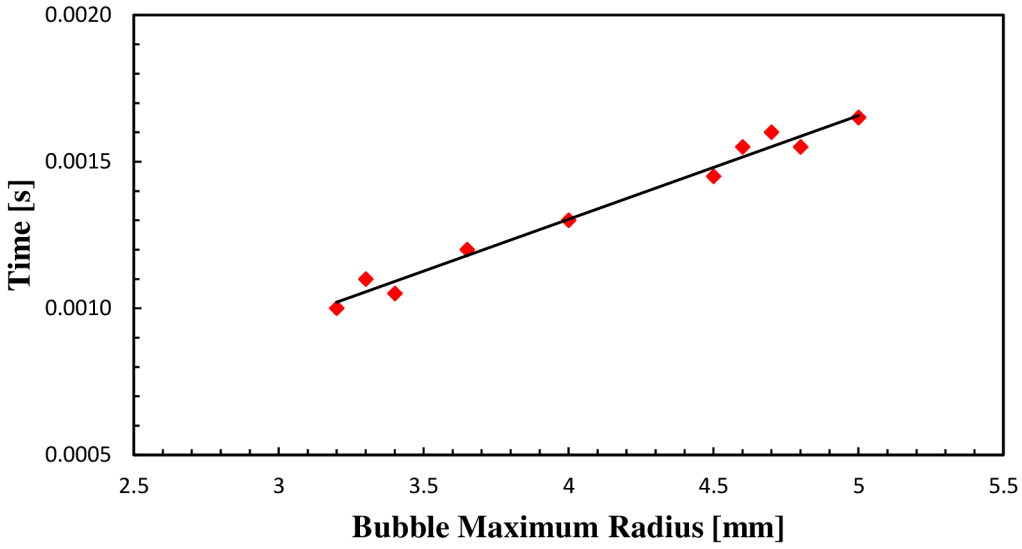

Figure 4-5. First cycle times of the bubbles.

In this thesis, several different values of the γ were used, mainly in the interval of $0.8 \leq \gamma \leq 2$. The process was captured by NanoSense MKIII camera, with 10000 fps and exposure of 10 μs. In figure you can see high speed photographs for difference dimensionless distances: γ= 1.94, γ = 1.59, γ = 0.83. Maximum radiuses R_{max} are 3.4 mm, 3.65 mm and 4.7 mm respectively. Distances L from the wall to the bubble center are 6.6 mm, 5.8mm and 3.9mm respectively. Maximum radiuses are reached at frames *a7, b12* and *c12* of Figure 4-6. After this, the bubble starts to shrink and collapse, due to the smaller inside pressure, after the collapse, the rebound is created. The cavitation microjet is formed because, the collapse velocity of the left side wall is bigger than on the right side, so jet goes in the direction of the wall. As you can see, for γ = 1.94 jet is happening after the bubble collapse at time of 1.2ms from the spark generation (*frame a13* - Figure 4-6). The collapse is almost ideally spherical and maximum rebound can be seen at the frame *a14*. From the pictures below, it is clearly visible that the microjet hits the wall during the first collapse for small γ.

`

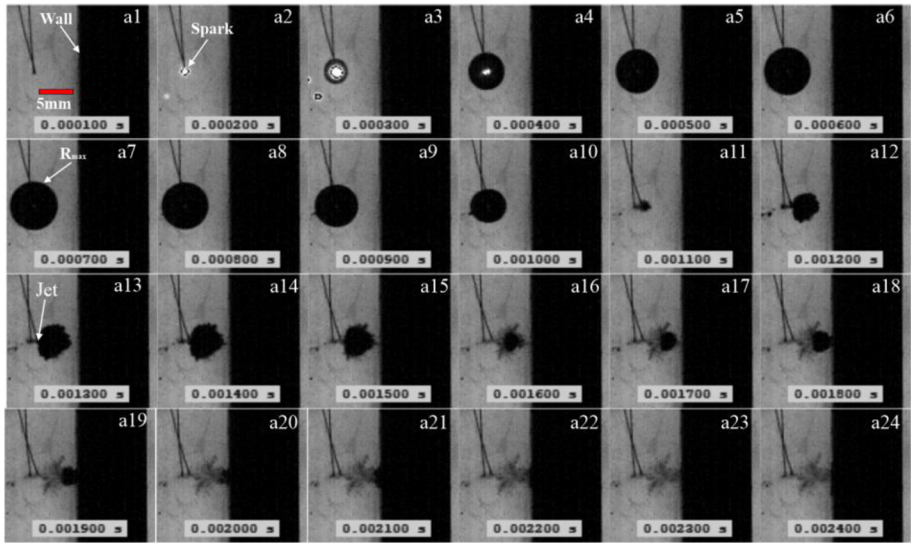

a. $\gamma = 1.94$; $R_{max} = 3.4$mm

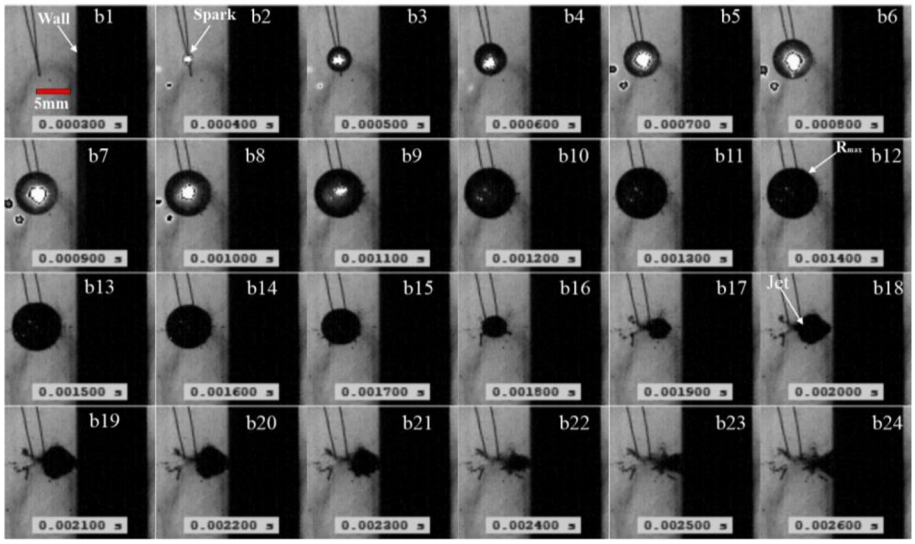

b. $\gamma = 1.59$; $R_{max} = 3.65$mm

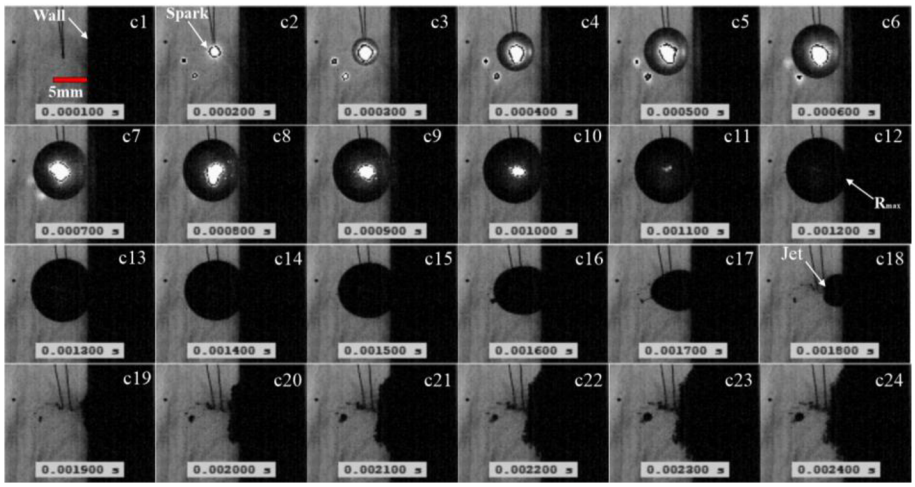

c. $\gamma = 0.83$; $R_{max} = 4.7$mm

Figure 4-6. CCD Camera images of bubble collapse during different values of "γ".

`

Figure 4-7 below represents maximum impact forces and maximum loading stress (pressure) of first and second collapse during different values of γ. The signals are received on the first PVDF sensor, which is closer to the impact. As it is visible, second collapse peaks are higher than the first collapse peaks on both charts during 1 < γ and values are practically in the same range. Impacts are increasing until γ=1.33 for the first collapse and until γ=1.25 for the second collapse respectively. It also has to be mentioned that second collapse impacts are higher than first at the point γ=1.25. There is a significant increase of maximum first collapse impacts from γ=1.25 to γ=1.33 and a dramatic decrease from γ=1.33 to γ=1.59. For γ=1.71 maximum impact values are again increased, following by a decrease through γ=1.78 and γ=1.88 after which forces and stresses are increasing significantly to the value of γ=1.94. The second collapse has similar characteristic values from γ=1.25, but in difference with the first collapse, from γ=1.94 it again decreases.

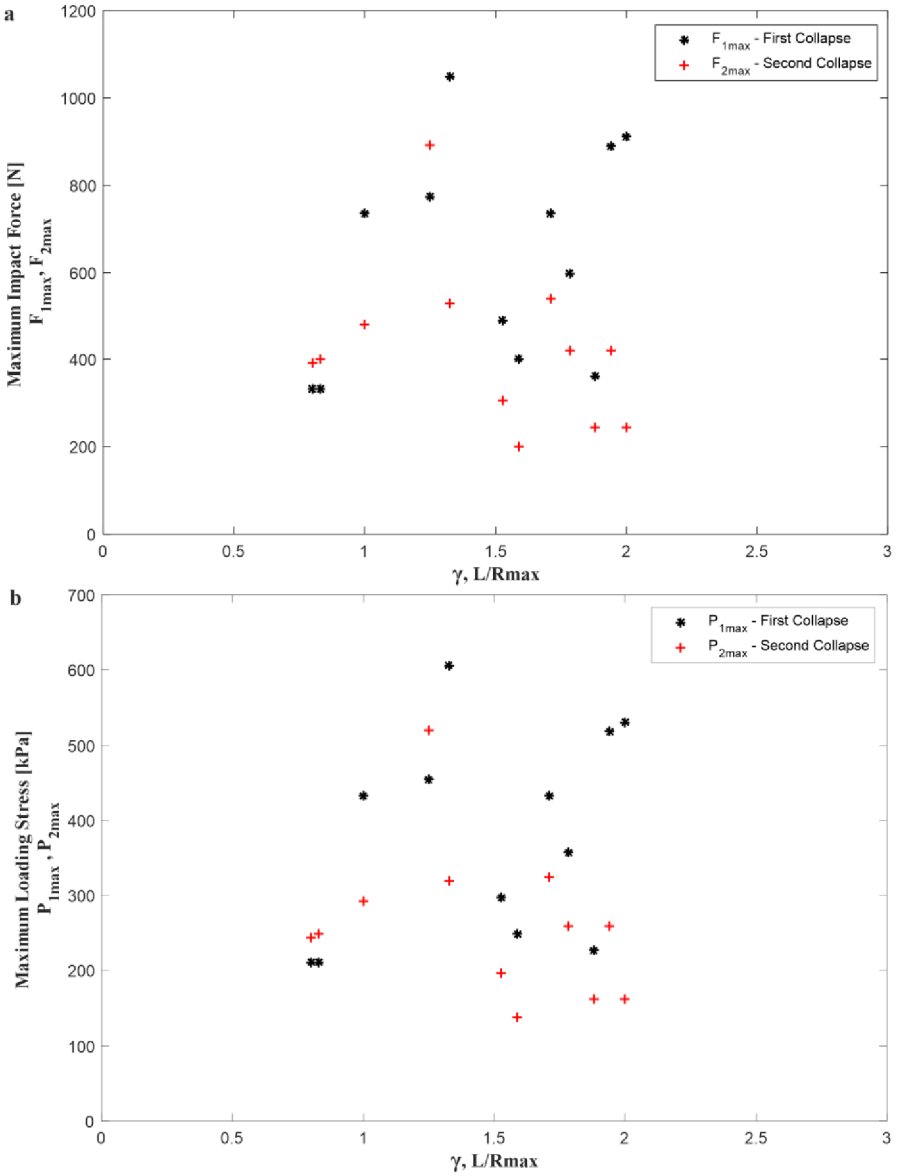

Figure 4-7. Maximum impact forces (a) and mechanical stresses (b) during first and second collapse – Sensor 1.

`

Figure 4-8 (a) an (b), again represents the maximum impact forces and loading stresses due to the first and second collapse, but in this case for second PVDF sensor, far from the spark generation. As it visible, impact forces and pressures for first collapse increase in the range $0.83 \leq \gamma \leq 1.33$, while second collapse increases from γ=0.83 until γ=1.25. After that, values on both charts decrease significantly until γ=1.59. From γ=1.59 impact forces and stresses during both collapses, have same characteristics as for 1st PVDF sensor, described above.

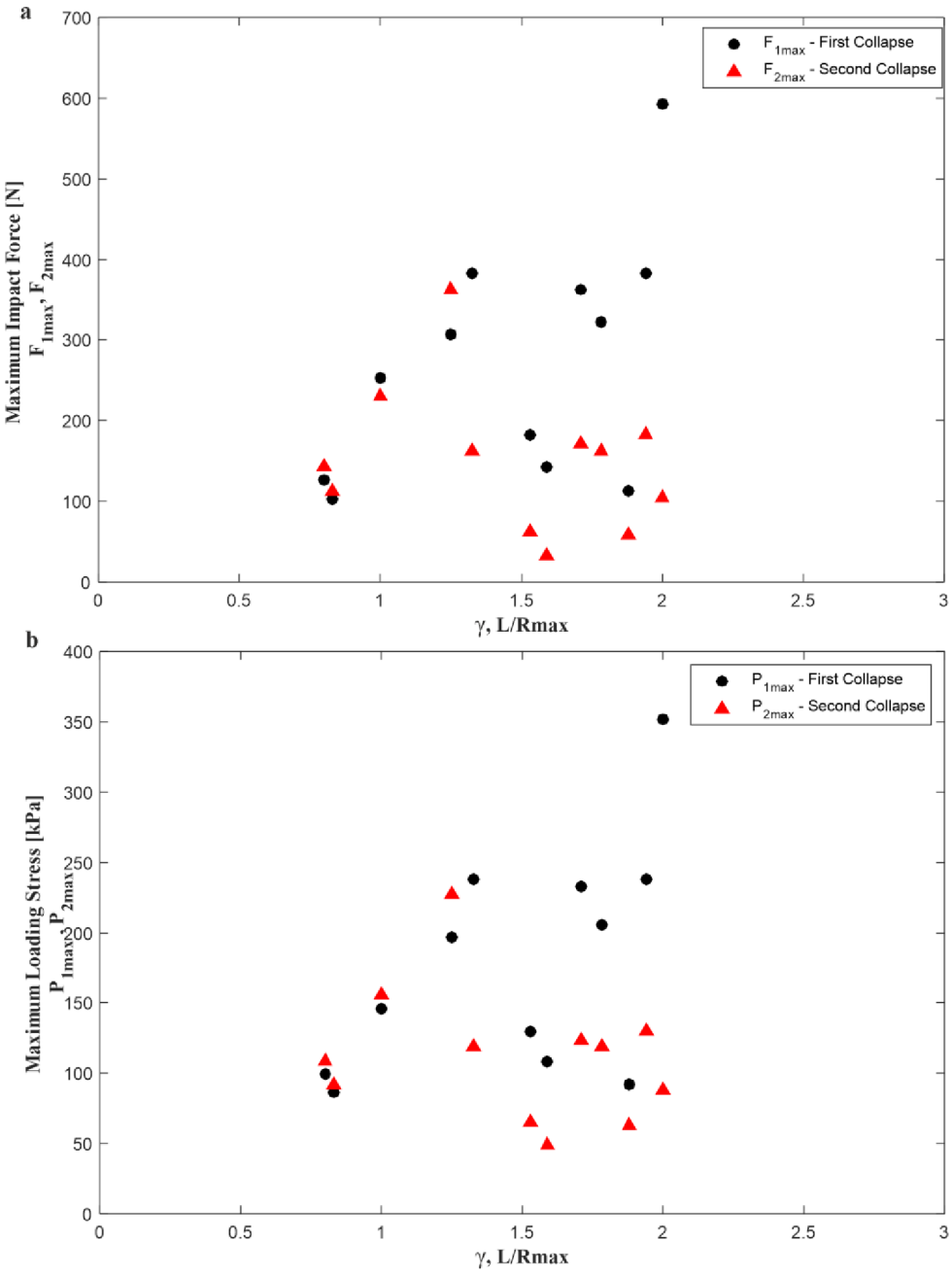

Figure 4-8. Maximum impact forces (a) and mechanical stresses (b) during first and second collapse – Sensor 2.

`

4.4.1 Dimensionless Stand-off Parameter $1.59 \leq \gamma \leq 2$

As microjets mostly occur during the parameter $\gamma \leq 2$ we will start to analyze results with the range of $1.59 \leq \gamma \leq 2$ and different ranges will also be discussed in following sections. In Figure 4-9 cavitation bubble has maximum radius $R_{max} = 4.8\ mm$ and distance from the wall is $L = 8.2\ mm$, so γ=1.71. It is visible that cavitation microjet is created practically instantaneously after the first collapse of the bubble around $\tau \approx 0.00175\ s$. The collapse is represented on the Figure 4-10 as the first peak. The second peak is due to the second collapse, or collapse of the rebound bubble. Time interval between those peaks is $\Delta\tau = 0.0008\ s$. It has to be mentioned that, after the second collapse which is around $\tau \approx 0.00257s$, another microjet occur, causing the third collapse of the deformed bubble.

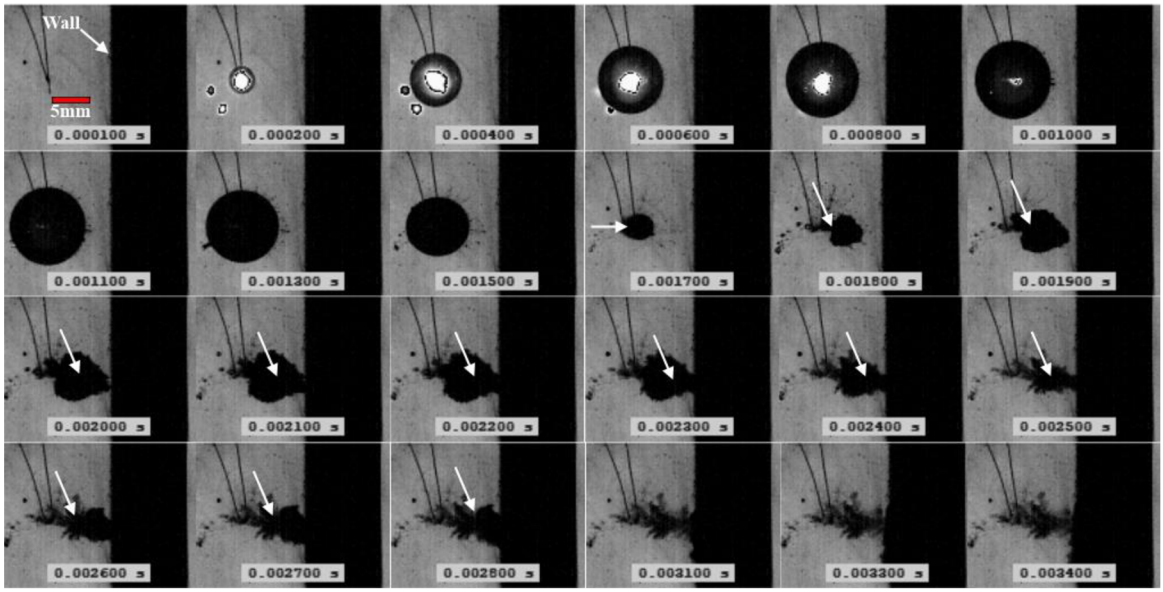

Figure 4-9. Bubble generation and collapse (γ=1.71).

Maximum stress captured by the 1st sensor PVDF during the first collapse is $P_{1max} = 432.9\ kPa$ and $P_2 = 324.5\ kPa$ during the second collapse respectively, while maximum forces are $F_1 = 734\ N$ for the first and $F_2 = 538\ N$ for the second respectively. Many authors mention that during these ranges, especially when gamma $\gamma > 1.5$ microjet impact is not significant as a stress and it is practically not measured or recognized in whole signal, however in their paper, Lou et al., [38] suspected that during γ =1.79 in second collapse there are two pressure peaks and the maximum peak is due to the microjet effect based on the water hammer formula. However, this assumption in these range of stand-off parameter is very rare and the second collapse signal with two peaks in mentioned ranges never occurred in this research for $1.59 \leq \gamma \leq 2$. However, I would like to discuss one more result, (it is not exactly proven, but is just an assumption), if we consider that microjet firstly occurs in the time of the first bubble collapse (and this is also assumed by Wang et al., [36]) and it might have small part in the signal received from this collapse and then look into the received maximum stress or force in Figure 4-7, we can see that the values which should been received in accordance with our model is a bit smaller, (*89 N* in case of force and *61 kPa* in case of stress), actual signal is higher and maybe this difference is caused by the microjet?! The same characteristic is captured during γ=1.78 and γ=1.33.

`

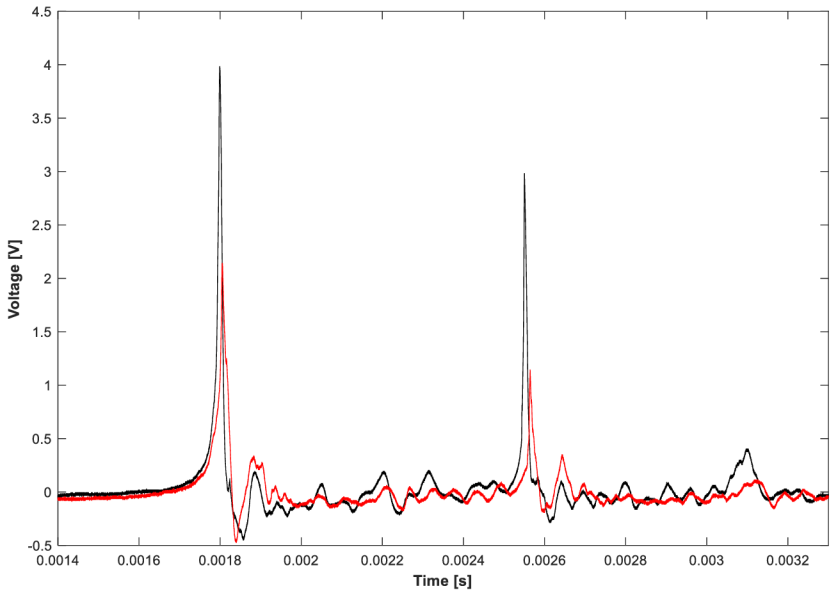

Figure 4-10. Received signal (γ=1.71).

Lastly, in all the experiments conducted in the range of $1.59 \leq \gamma \leq 2$ and not only in these distances, there are some very small peaks after the first and second collapse of the bubble, which might be due to the shock waves in accordance with Tong et al.,[22].

4.4.2 Dimensionless Stand-off Parameter $1.2 \leq \gamma \leq 1.55$

In the range of $1.2 \leq \gamma \leq 1.55$ general characteristics of the signal are similar to the previously discussed distances. In this case, we still have large and longer-lasting pressure caused mainly by shock wave emissions. In Figure 4-11, proximity parameter γ= 1.25, with maximum bubble radius $R_{max} = 4.8\ mm$ and distance from the wall $L = 6\ mm$. The shape of the measured signal for first collapse is similar to the results with similar stand-off distances, from different authors: Tong et al.,[22], Shaw et al., [41], Wang et al., [36], etc. Numerical simulation from Tong et al.,[22] indicates the behavior of the bubble and in accordance with it, jet impact is definitely before the bubble reaches its minimum volume.

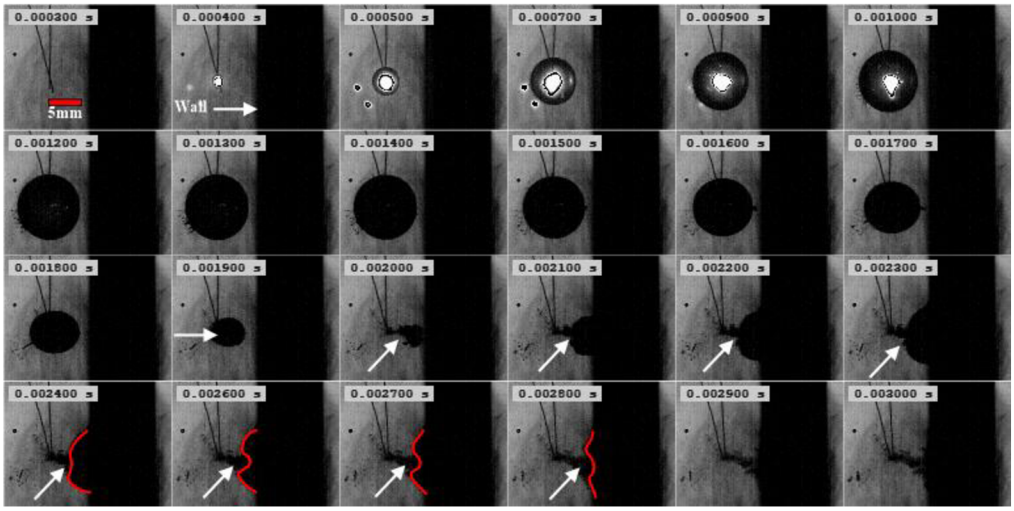

Figure 4-11. Bubble generation and collapse (γ=1.25).

`

While, in the experiment of Tong et al.,[22] jet impact is calculated to be 5 μs before the dominant pressure loading, in our case corresponding time should be 18.45 μs (bubble radius in this case is 3.7 times bigger than in the study of Tong et al.,[22]) which is indicated by the arrow in Figure 4-12, but there is no significant stress or force recorded in this time. Time difference between two peaks approximately $\Delta\tau = 0.0009s$.

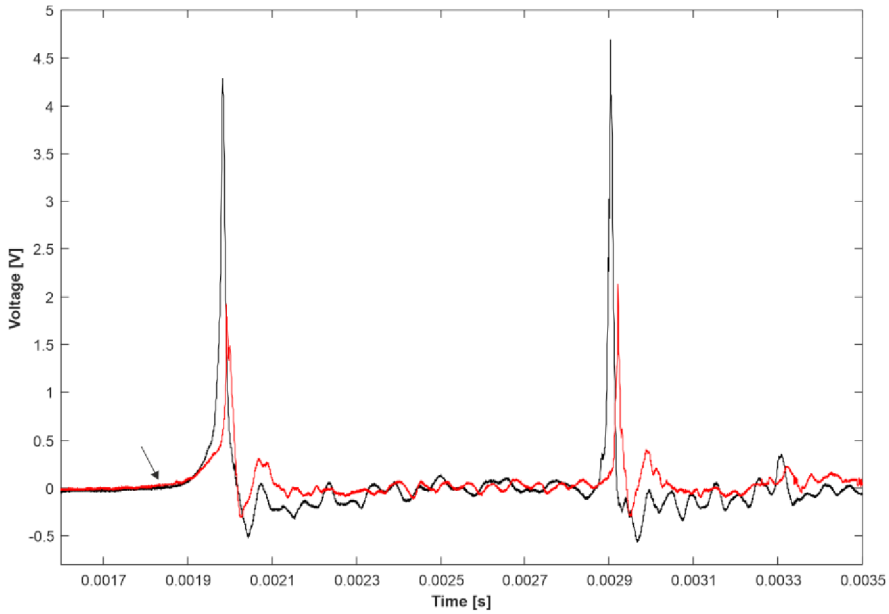

Figure 4-12. Received signal (γ=1.25).

As it is clear from the Figure 4-12 the amplitude of the second peak is higher than the first peak, in accordance with this, the maximum stress captured by the PVDF 1st sensor during the first collapse is P_{1max}=*454.5 kPa* and P_{2max} = *606.2 kPa* during the second collapse respectively, while maximum impact forces are F_{1max} = *774 N* for first and F_{2max} = *838 N* for the second respectively. It is interesting because during the second collapse for this try and also for γ=1.33 (Figure 4-13) there are two peaks which have not been captured in higher stand-off distances previously.

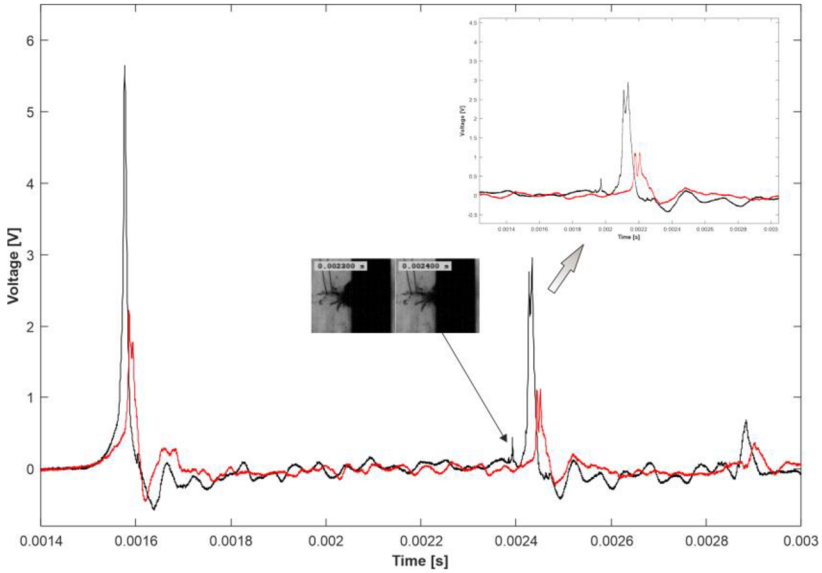

Figure 4-13. Received signal (γ=1.33).

`

The first peak most probably is due to the splash effect impact, caused by a microjet, while the second peak might be due to the acceleration of the flow towards the torus. Also, around the time $\tau \approx 0.0024\ s$, there is a small peak indicated by the arrow with values of $F \approx 25\ N$ and $P \approx 48\ kPa$, which corresponds to the jet impact in the photos captured on CCD camera and if we consider that splash effect is caused by the jet, this small peak may be the value of the jet impact. Furthermore, during this value of dimensionless stand-off parameter, the difference between the values of theoretical and experimental collapse of the bubble are approximately $\Delta F = 25\ N$. This might be just a coincidence, but still worth mentioning. The shape of the second collapse signal is very similar to what has been discussed by many authors during $0.6 < \gamma < 1$, which also will be discussed in this thesis in the following section. The amplitude of the force due of the first peak is $F_{1max} \approx 480\ N$ and applied stress is approximately $P_{1max} \approx 292\ kPa$, while for the second peak it is higher and equals $F_{2max} \approx 520\ N$ and stress $P_{2max} \approx 314\ kPa$.

4.4.3 Dimensionless Stand-off Parameter $0.8 \leq \gamma < 1$

In this thesis, the most important range of ratios between the distance from the wall and the maximum bubble radius are $0.8 \leq \gamma \leq 1$. Tong et al.,[22], Shaw et al.,[41], Wang et al., [36] and other authors have made different experiments to capture, describe and discuss the behavior of the bubble collapse this close to the wall. The most important feature which is similar to above-mentioned authors' works and this thesis, is the shape of the bubble collapse signal, especially double peaks during the first collapse. In Figure 4-14, you can see bubble collapse of the cavitation bubble 3.6mm from the wall, with maximum radius of $R_{max} = 4.5mm$, so that the value $\gamma = 0.8$. It is not discussed in this thesis, but according to other researches, when the stand-off parameter is even smaller, the difference between the amplitudes of the dominant pressure and the second peak is higher. In this case, that the dominant pressure peak is decreased and is practically the identical to the other peak. The maximum impact force captured in correspondence with these peaks is $F_{max} = 332.6\ N$.

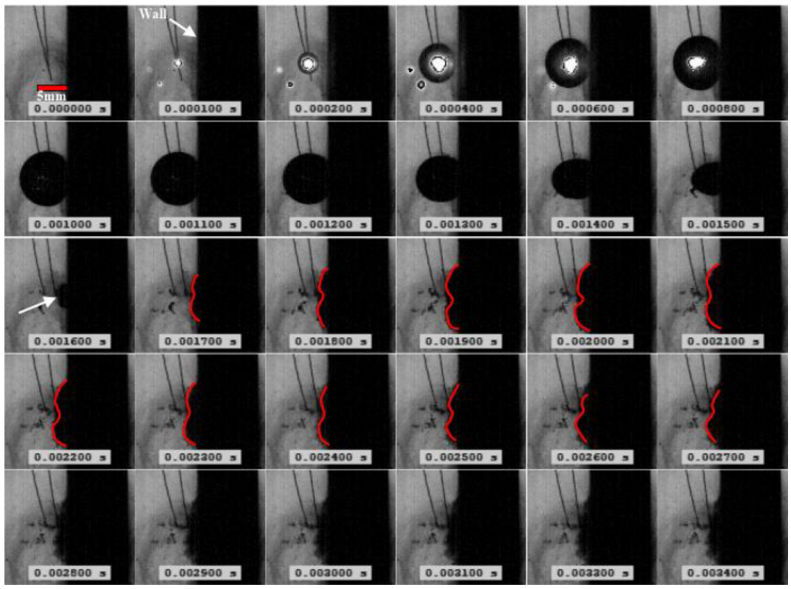

Figure 4-14. Bubble generation and collapse (γ=0.8).

`

An interesting process is that a toroidal bubble is created just after the microjet impact and splash starts to move away from the boundary and has a similar shape as a mushroom [22]. So, the first peak is connected to the splash effect based on microjet and then it is accompanied by the shock waves, while the second peak might be due to the acceleration of the flow towards the torus, which has been already mentioned. It is worth mentioning the significant impact of the jet itself, which is now even sooner than it was discussed in the previous section, still can't be measured.

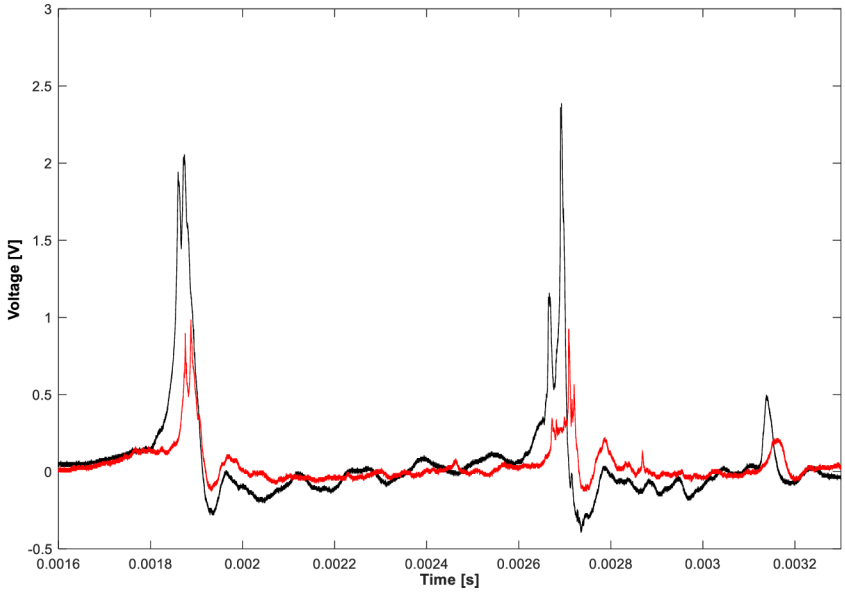

Figure 4-15. Received signal (γ=0.8).

The maximum value of the loading stress captured by the 1st PVDF sensor during the 1st collapse is P_{max}=*211 kPa*. It is interesting that, the same kind of relationship is repeating during the second collapse of the bubble, but now, the second peak is definitely higher than the first (caused by the splash impact).

5. CONCLUSION

This thesis aimed to determine, if it is possible or not to identify the impacts of cavitation microjet and shock waves separately, using PVDF sensors placed on a metal plate. The first chapter includes information about the fundamental terms in cavitation, while the second chapter includes a review of specific literature related to PVDF sensors and cavitation bubble generation and its impact on the nearby rigid boundary. The third chapter describes the methodology, experimental setup with used equipment, the results of which are discussed in the next chapter. Dimensionless stand-off (proximity) parameter has a big influence on the behavior, generation and collapse of the cavitation bubble, accompanied by shock waves, microjet, or splash effects. In this thesis, three ranges of dimensionless parameter γ are analyzed.

`

For $1.59 \leq \gamma \leq 2$ no significant impact due to microjet is recorded. However, there is a small difference between the theoretically assumed values of impact forces and loading stresses, which might be caused by the microjet. Additionally, right after the first and second collapse, there are very tiny peaks, which may be caused due to shockwaves. In this range, impact forces are loading stresses (pressures) are increasing until γ=1.71, from there they decrease until γ=1.88 and then still suddenly increase. General characteristics of the bubble are practically identical in the range of $1.2 \leq \gamma \leq 1.55$, Here it is even more visible that jet impact is before the bubble reaches its minimum volume. There is a sudden increase of the impact from γ=1.25 to γ=1.33, while during γ=1.25 second collapse of the bubble is higher than the first collapse and the signal has some small peaks. Interestingly, during γ=1.33, there is a well-defined shape of the signal two peaks during the second collapse and the peaks can be caused by the splash effect due to microjet impact and the second might be due to the bubble ring collapse. This phenomenon mostly occurs during the first collapse in the range of $0.6 \leq \gamma \leq 1$. Lastly, it is not frequent in this research but as some authors suggest, sometimes it is possible to have a higher second collapse impact than for the first collapse.

For us, in this thesis, the most important variation of the stand-off parameter γ is when $0.8 \leq \gamma \leq 1$. Similarly, to other researchers, in this paper too, there are two peaks captured during the first and second collapse. The toroidal bubble and splash are formed, after the impact of cavitation microjet, so that radial outflow and inflow meet each other and when splash moves from the boundary it has a shape similar to a mushroom. Shock waves accompany this splash effect and the first peak might be considered as the impact of these shock waves, while the second peak is most probably due to the acceleration of flow, in the direction of the torus. Despite all this, the exact impact of the jet alone, still can't be detected. Despite all this, the exact impact of the jet alone, still can't be detected. Several other researchers have conducted experiments on this phenomenon in practically the same range of γ. Sarkar et al.,[39] in 2018, made a number of numerical investigations about the dynamics of pressure loading caused by the cavitation bubble collapse. For the $\gamma = 0.8$ they also received two pressure peaks. There, they mention that the first peak is due to the cavitation microjet while the stronger second is the result of the collapse bubble ring or torus, more specifically, due to the interacting shock waves caused by the collapse of the bubble ring [39]. Chahine et al.,[40], have also made similar research, for the stand-off parameter $\gamma = 0.75$. In this article, they also outline the same phenomenon, that the second peak, caused by the ring collapse is higher than the first one, caused by the microjet accompanied by the splash effect. Based on all the information above, we can also say that, it might not be able to detect the exact impact of the cavitation microjet, with this kind of setup used in this master's thesis, but we can still receive information about the splash effect caused directly by the jet and other accompanying phenomena.

Lastly, I would like to say that, area of the PVDF sensor is much bigger than the area of the impact, the information about forces and stress is total collective and considered to be applied equally to all sensitive surface of the film, because the relationship between the erosion and pit sizes are quite complicated in some ways and studies are still incomplete [36].

`

REFERENCES

[1] The Editors of Encyclopaedia Britannica. *Cavitation.* Encyclopædia Britannica [online]. 2018. Dostupné z: https://www.britannica.com/science/cavitation

[2] CHAHINE, Georges & KIM, Ki-Han & FRANC, Jean-Pierre & KARIMI, Ayat. (2014). *Advanced Experimental and Numerical Techniques for Cavitation Erosion Prediction*. 10.1007/978-94-017-8539-6.

[3] FRANC, Jean-Pierre & MICHEL, J.-M. (2005). *Fundamentals of Cavitation*. Fluid Mechanics and Its Applications. 76. 10.1007/1-4020-2233-6.

[4] ROY, Samir. *Modeling and analysis of material behavior during cavitation erosion. Materials.* Université Grenoble Alpes, 2015. English. NNT: 2015GREAI081. tel-01267573

[5] MÜLLER, Milos. *Dynamic behavior of cavitation bubbles generated by laser*. Liberec: Technical University of Liberec, 2008. 108 pp. Knihovnicka.cz. ISBN 978-80-7372-241-8..

[6] PHAN, Menghout. *Piezoelectric film sensors for the cavitation impact measurement.* Technical University of Liberec, Liberec, 2020.

[7] YASUI, Kyuichi. *Acoustic Cavitation and Bubble Dynamics [online]*. 2018. ISBN 978-3-319-68236-5. Dostupné z: doi:10.1007/978-3-319-68237-2

[8] DURAN, M.M. Campo "*Investigation of the Cavitation Aggressiveness Using PVDF Sensors"*. Technical University of Liberec, Liberec, 2018.

[9] KNAPP, R. T., DAILY J. W. and HAMMITT. F. G. *Cavitation*, New York: McGraw-Hill, 1970.

[10] KLIMES, Mike. *Understanding and avoiding pump cavitation.* Flow Control Network [online]. 2017, 1. Dostupné z: https://www.flowcontrolnetwork.com/pumps-motors-drives/article/15563623/understanding-and-avoiding-pump-cavitation

[11] MAXIME, Binama & MUHIRWA, Alexis & BISENGIMANA, Emmanuel. (2016). *Cavitation Effects in Centrifugal Pumps-A Review*. Int. Journal of Engineering Research and Applications. 6. 2248-962252.

[12] KHURANA, S. & NAVTEJ, & SINGH, Hardeep. (2012). *Effect of cavitation on hydraulic turbines - a review*. Int J Curr Eng Technol. 2. 172-177.

[13] BRENNEN, C. E. *An Introduction to Cavitation Fundamentals, in Cavitation: Turbo-machinery & Medical Applications*. University of Warwick, UK, 2011.

[14] PISHCHALNIKOV, Y. A. and SAPOZHNIKOV, O. A. *"Cavitation bubble cluster activity in the breakage of stones by shock wave lithotripsy"*. The Journal of the Acoustical Society of America, vol. 111, no. 5, pp. 24-61, 2002.

[15] BRENNEN, C. E. "*Cavitation in medicine"*. Interface Focus, vol. 5, no. 5, 2015.

[16] SOYAMA, Hitoshi & ODHIAMBO, Dan & SAITO, Kenichi. (2006). *Cavitation Shotless Peening for Improvement of Fatigue Strength*. doi:10.1002/3527606580.ch55.

[17] DULAR, T. GRIESSLER-BULC, I. GUTIEREZ, E. HEATH, T. KOSJEK, A.K. KLEMENČIČ, M. ODER, M. PETKOVŠEK, N. RAČKI, M. RAVNIKAR, A. ŠARC, B. ŠIROK, M. ZUPANC, M. ŽITNIK, B. KOMPARE. *Use of hydrodynamiccavitation in (waste)water treatment.* Ultrasonics Sonochemistry (2015), Dostupné z: doi:10.1016/j.ultsonch.2015.10.010

[18] FRANC, J. P. *The rayleigh-plesset equation: A simple and powerful tool to understand various aspects of cavitation*. CISM Int. Cent. Mech. Sci. Courses Lect., vol. 496, pp. 1–41, 2007.

[19] LORD RAYLEIGH. *On the pressure developed in a liquid during the collapse of a spherical cavity*, Philos. Mag. Ser. 6. 34 (1917) 94–98. Dostupné z doi:10.1080/14786440808635681.
[20] KORNFELD, M., SUVOROV, L. *On the Destructive Action of Cavitation*, J. Appl. Phys. 15 (1944) 495. Dostupné z doi:10.1063/1.1707461.
[21] SAI, R.A. *The Improvement of the cavitation resistance of technical surfaces using high power laser Pulses.* Technical University of Liberec, Liberec, 2020.
[22] TONG, R., SCHIFFERS, W., SHAW, S., BLAKE, J., & EMMONY, D. (1999). The role of 'splashing' in the collapse of a laser-generated cavity near a rigid boundary. Journal of Fluid Mechanics, 380, 339-361. doi:10.1017/S0022112098003589
[23] B. K. Sreedhar, S. K. Albert, and A. B. Pandit. "*Cavitation damage: Theory and measurements – A review*," Wear, vol. 372–373, pp. 177–196, 2017.
[24] AIDOO, E.O. *Material response on the cavitation bubble collapses.* Technical University of Liberec, Liberec, 2018.
[25] LUO, J., NIU, Z. *Jet and Shock Wave from Collapse of Two Cavitation Bubbles*. Sci Rep 9, 1352 (2019). Dostupné z https://doi.org/10.1038/s41598-018-37868-x
[26] *Piezo Film Sensors Technical Manual (1999),* Norrsitown, Measurement Specialties.
[27] SESSLER, G.M. (1981). *Piezoelectricity in Polyvinylidene Fluoride*. Journal of The Acoustical Society of America - J ACOUST SOC AMER. 70. 10.1121/1.387225.
[28] HU, Y.; KANG, W.; FANG, Y.; XIE, L.; QIU, L.; JIN, T. *Piezoelectric Poly(vinylidene fluoride) (PVDF) Polymer-Based Sensor for Wrist Motion Signal Detection*. Appl. Sci. 2018, 8, 836. https://doi.org/10.3390/app8050836
[29] CONG, J.; JING, J.; ChEN, C.; DAI, Z. *Development of a PVDF Sensor Array for Measurement of the Dynamic Pressure Field of the Blade Tip in an Axial Flow Compressor.* Sensors 2019, 19, 1404. https://doi.org/10.3390/s19061404
[30] WANG, YC., HUANG, CH., LEE, YC. et al. *Development of a PVDF sensor array for measurement of the impulsive pressure generated by cavitation bubble collapse.* Exp Fluids 41, 365–373 (2006). https://doi.org/10.1007/s00348-006-0135-8
[31] TE Connectivity. *DT SERIES ELEMENTS WITH LEAD ATTACHMENT*. SENSOR SOLUTIONS /// DT Series Rev 1 07/2017
[32] KOTIAN, Kunal. *Detection of in-plane stress waves with Polyvinylidene Fluoride (PVDF) sensors.* (2013).
[33] XU, Wei-lin & LI, Nai-wen. (2008). A High-Speed Photographic Study of Ultrasonic Cavitation Near Rigid Boundary. Journal of Hydrodynamics - J HYDRODYN. 20. 637-644. https://doi.org/10.1016/S1001-6058(08)60106-7.
[34] SHAN, MINGLEI & CHEN, Bingyan & YAO, Cheng & HAN, Qingbang & ZHU, Changping & YANG, Yu. (2019). *Electric characteristic and cavitation bubble dynamics using underwater pulsed discharge.* Plasma Science and Technology. 21. 074002. https://doi.org/10.1088/2058-6272/ab0b62.
[35] SCHOVANEC, Petr & GAREN, Walter & Koch, S. & NEU, W. & DANCOVA, Petra & JASIKOVA, Darina & KOTEK, Michal & KOPECKÝ,Václav. (2019). *Laser generated plasma followed by shocks and increasing cavitation bubble in a mini-glass tube*. ACC Journal. 25. 58-67. https://doi.org/10.15240/tul/004/2019-1-005.
[36] WANG, Yi-Chun, & CHEN, Yu-Wen. *Application of piezoelectric PVDF film to the measurement of impulsive forces generated by cavitation bubble collapse near a solid boundary*. Experimental Thermal and Fluid Science, Volume 32, Issue 2, 2007, Pages 403-414, ISSN 0894-1777, https://doi.org/10.1016/j.expthermflusci.2007.05.003.

`

[37] HUJER, J. and MULLER, M. *Calibration of PVDF Film Transducers for the Cavitation Impact Measurement.* EPJ Web of Conferences, vol. 180, p. 02036, 2018.

[38] LUO, J.; XU, W.; DENG, J.; ZHAI, Y.; ZHANG, Q. *Experimental Study on the Impact Characteristics of Cavitation Bubble Collapse on a Wall*. Water 2018, 10, 1262. https://doi.org/10.3390/w10091262

[39] SARKAR Prasanta, GHIGLIOTTI Giovanni, FIVEL Marc C., FRANC Jean Pierre. *Numerical investigation of the dynamics of pressure loading on a solid boundary from a collapsing cavitation bubble*. 10th International Symposium on Cavitation - CAV2018, May2018, Baltimore, United States. hal-02066205

[40] CHANINE, Georges & HSIAO, Chao-Tsung. (2015). *Modelling cavitation erosion using fluid – material interaction simulations.* Interface focus: a theme supplement of Journal of the Royal Society interface. 5: 20150016. 10.1098/rsfs.2015.0016.

[41] SHAW SJ, SCHIFFERS WP, EMMONY DC. *Experimental observations of the stress experienced by a solid surface when a laser-created bubble oscillates in its vicinity*. J Acoust Soc Am. 2001 Oct;110(4):1822-7. doi: 10.1121/1.1397358. PMID: 11681363

`

APPENDIX

Table A.1 Calibration data of the 1st PVDF sensor

PVDF Sensor - 1										
Trial	Mass (g)	h_1 (mm)	h_2 (mm)	v_1 (m/s)	v_2 (m/s)	t_1 (μs)	t_2 (μs)	τ (μs)	Vmax (V)	Fmax (N)
1	0.438	400	147	2.80	1.70	37.5	62.5	25	1.1	157.68
2	0.438	400	191	2.80	1.94	37.5	62.5	25	1.14	167.33
3	0.438	400	181	2.80	1.88	38	61.5	23.5	1.03	174.67
4	0.438	400	140	2.80	1.66	36	64	28	1.03	139.49
5	0.438	400	166	2.80	1.80	38	61.5	23.5	1.13	171.70
1	0.696	400	160	2.80	1.77	38	64	26	1.52	247.7
2	0.696	400	209	2.80	2.02	38	64	26	1.61	258.4
3	0.696	400	188	2.80	1.92	38	64.5	26.5	1.53	248.04
4	0.696	400	185	2.80	1.91	38	65	27	1.53	242.65
5	0.696	400	155	2.80	1.74	38	64	26	1.4	243.35
1	1.250	400	156	2.80	1.75	38	69	31	2.07	367.01
2	1.250	400	147	2.80	1.70	38	67	29	2.28	387.90
3	1.250	400	178	2.80	1.87	38	67	29	2.26	402.60
4	1.250	400	174	2.80	1.85	38	70	32	2.2	363.21
5	1.250	400	144	2.80	1.68	38	67	29	2.3	393.18

Table A.2 Calibration data of the 2nd PVDF sensor

PVDF Sensor - 2										
Trial	Mass (g)	h_1 (mm)	h_2 (mm)	v_1 (m/s)	v_2 (m/s)	t_1 (μs)	t_2 (μs)	τ (μs)	Vmax (V)	Fmax (N)
1	0.438	400	166	2.80	1.80	38	61.5	23.5	1.13	171.70
2	0.438	400	185	2.80	1.91	38	62.5	24.5	1.12	168.28
3	0.438	400	181	2.80	1.88	38	61.5	23.5	1.03	174.67
4	0.438	400	170	2.80	1.83	38	62	24	1.17	168.91
5	0.438	400	185	2.80	1.95	38	62	24	1.18	173.27
1	0.696	400	166	2.80	1.91	38	64.5	26.5	1.52	247.23
2	0.696	400	175	2.80	1.80	38	63.5	25.5	1.53	251.44
3	0.696	400	187	2.80	1.85	38	63	25	1.62	259.15
4	0.696	400	191	2.80	1.92	38	63	25	1.71	262.63
5	0.696	400	155	2.80	1.94	38	64.5	26.5	1.57	248.84
1	1.250	400	177	2.80	1.86	38	65.5	27.5	2.58	424.087
2	1.250	400	160	2.80	1.77	38	66	28	2.3	408.3221
3	1.250	400	145	2.80	1.69	38	69	31	2.07	361.9445
4	1.250	400	162	2.80	1.78	38	66	28	2.23	409.3077
5	1.250	400	150	2.80	1.72	38	67	29	2.13	389.3919

`

Table A.3 Maximum Impact Forces and Mechanical Stresses on 1st Sensor

PVDF Sensor - 1							
γ [-]	R_{max} (mm)	V_{1max} (V)	F_{1max} (N)	P_{1max} (Pa)	V_{2max} (V)	F_{2max} (N)	P_{2max} (Pa)
0.80	4.50	1.95	332.67	211039	2.25	391.49	243506
0.83	4.70	1.95	332.67	2110389	2.30	401.29	248918
1.00	4.50	4	734.63	432900	2.70	479.73	292208
1.25	4.80	4.2	773.84	454545	4.80	891.49	519481
1.33	4.60	5.6	1048.35	606060	2.95	528.75	319264
1.53	3.80	2.75	489.53	297619	1.82	307.18	196970
1.59	3.65	2.3	401.29	248918	1.28	201.29	138528
1.71	4.80	4	734.63	432900	3.00	538.55	324675
1.78	4.60	3.3	597.37	357143	2.40	420.90	259740
1.88	3.20	2.1	362.08	227273	1.50	244.43	162338
1.94	3.40	4.79	889.53	518398	2.40	420.90	259740
2.00	5.00	4.9	911.10	530303	1.50	244.43	162338
3.36	3.30	1.42	232.67	155844	3.30	597.37	357143

Table A.4 Maximum Impact Forces and Mechanical Stresses on 2nd Sensor

PVDF Sensor - 2							
γ [-]	R_{max} (mm)	V_{1max} (V)	F_{1max} (N)	P_{1max} (Pa)	V_{2max} (V)	F_{2max} (N)	P_{2max} (Pa)
0.80	4.50	0.92	126.76	99567	1	142.76	108225
0.83	4.70	0.8	102.76	86580	0.85	112.76	91991
1.00	4.50	1.35	252.76	146104	1.44	230.76	155844
1.25	4.80	1.82	306.76	196970	2.1	362.76	227273
1.33	4.60	2.2	382.76	238095	1.1	162.76	119048
1.53	3.80	1.2	182.76	129870	0.6	62.76	64935
1.59	3.65	1	142.76	108225	0.45	32.76	48701
1.71	4.80	2.15	362.76	232684	1.14	170.76	123377
1.78	4.60	1.9	322.76	205628	1.1	162.76	119048
1.88	3.20	0.85	112.76	91991	0.58	58.76	62771
1.94	3.40	2.2	382.76	238095	1.2	182.76	129870
2.00	5.00	3.25	592.76	351732	0.81	104.76	87662
3.36	3.30	1.48	238.76	160173	1	142.76	108225

`

Table A.5 Theoretical and experimental values of impact forces and applied mechanical stresses.

γ [-]	R_{max} (mm)	R_2/R_1 [-]	F_{1Exp} [N]	F_{12Exp} [N]	F_{1Model} [N]	P_{1Exp} [Pa]	P_{12Exp} [Pa]	P_{1Model} [Pa]
0.80	4.50	5.2	332.67	126.76	661.97	211039	99567	519740
0.83	4.70	4.7	332.67	102.76	487.45	211039	86580	410700
1.00	4.50	3.98	734.63	252.76	846.31	432900	146104	581169
1.25	4.80	2.73	773.84	306.76	838.48	454545	196970	538384
1.33	4.60	2.67	1048.35	382.76	1022.78	606061	238095	636222
1.53	3.80	2.86	489.53	182.76	523.07	297619	129870	371697
1.59	3.65	2.86	401.29	142.76	408.59	248918	108225	309748
1.71	4.80	1.73	734.63	362.76	645.51	432900	232684	371658
1.78	4.60	1.73	597.37	322.76	558.93	357143	205628	356087
1.88	3.20	2.73	362.08	112.76	308.21	227273	91991	251443
1.94	3.40	2.39	889.53	382.76	916.30	518398	238095	569986
2.00	5.00	1.26	911.10	592.76	748.43	530303	351732	436147
3.36	3.30	1.02	232.67	238.76	243.06	155844	160173	163059

F_{1Exp} – Force received during experiment by First Sensor (First Collapse)

F_{12Exp} – Force received during experiment by Second Sensor (First Collapse)

P_{1Exp} – Maximum mechanical stress during experiment by First Sensor (First Collapse)

P_{2Exp} – Maximum mechanical stress during experiment by Second Sensor (First Collapse)